aerospace

MDPI

Article

A Thermal-Environment-Informed Evaluation Index for Particle Combustion in Solid Rocket Ramjet Afterburner

Delei Shi, Lin Sun *, Futing Bao, Xiaoyu Lei and Chenmin Gao

National Key Laboratory of Solid Rocket Propulsion, Northwestern Polytechnical University, Xi'an 710072, China; shidelei@mail.nwpu.edu.cn (D.S.); ftbao@nwpu.edu.cn (F.B.); leixiaoyu@mail.nwpu.edu.cn (X.L.); gaochenmin@mail.nwpu.edu.cn (C.G.)

* Correspondence: sunlin@nwpu.edu.cn

Abstract

Efficient particle combustion is crucial for improving the overall performance of solid rocket ramjets. However, particle combustion is jointly constrained by multiple environmental factors, such as oxidizer supply, gas–solid transport, and residence characteristics, which are difficult to characterize using conventional mixing-ratio-based evaluations fully. To provide a diagnostic evaluation of particle combustion potential under complex flow-field organization during design and optimization, a thermal-environment-informed particle combustion index I_{TPCI} is proposed in this study. The index incorporates oxidizer availability, particle–oxidizer transport, residence-related effects, gas thermal environment, and particle thermal reactivity, and is intended to indicate regions where particle oxidizer-consumption capability can be retained under favorable thermochemical conditions. The reacting duct case shows that I_{TPCI} provides a combustion-potential-oriented description of particle consumption. In the canonical jet-interaction flow, the conventional mixing degree mainly identifies shear-layer-dominated transport boundaries, while I_{TPCI} emphasizes the regions with particle-consumption potential. Application to the afterburner further shows that particle combustion potential is governed by the match among oxidizer supply, particle transport, residence condition, and thermal environment. The head region has favorable thermal and residence conditions but remains oxygen-lean, whereas the downstream regions receive additional oxidizer but are constrained by nonuniform oxygen–particle distributions, thermal environment, and residence time. In the pulsed-jet cases, the variation of I_{TPCI} provides a diagnostic interpretation of changes in particle source-term distribution. For the present configuration, upstream pulsed actuation mainly enhances the head-region response, and the selected case increases the full-domain gaseous-product source term associated with boron combustion by 2.96%. These results indicate that the proposed index can support combustion-potential diagnosis and flow-control assessment in solid rocket ramjet afterburners.

Keywords: solid ramjet; thermal environment; fuel-rich gas; combustion organization; mixing

Check for updates

Academic Editor: James 'Chris' Thomas

Received: 15 June 2026
Revised: 22 July 2026
Accepted: 28 July 2026
Published: 31 July 2026

Copyright: © 2026 by the authors. Licensee MDPI, Basel, Switzerland. This article is an open access article distributed under the terms and conditions of the Creative Commons Attribution (CC BY) license.

1. Introduction

To meet the propulsion demands of hypersonic vehicles, the solid rocket ramjet has gradually become an ideal power system due to its high specific impulse and capability to provide cruise thrust [1,2]. In a solid rocket ramjet, the conversion of the propellant's chemical energy into thermal energy primarily occurs within the afterburner. The flow inside the afterburner can be characterized as interactions and mixing among multiple

intersecting jets. Since the fuel and oxidizer are not premixed, combustion mainly takes place in the "transition region", where the mixing between the two phases is relatively uniform. Therefore, enhancing the particle mixing between the oxidizer and fuel is a crucial approach to improving the heat-release capability of the motor [3,4].

To enhance the mixing and combustion performance of solid rocket ramjets without altering their general structural framework or propellant properties, researchers have conducted extensive studies on the design of mixing enhancement devices. Current research primarily focuses on passive mixing enhancement devices, with an emphasis on the arrangement and optimization of components such as cavities, struts, and wedges. The most common approach involves designing various cavity structures within the afterburner to slow down the gas flow, thereby entraining particles into the recirculation zone and prolonging their residence time [5,6]. While struts and splitter plates can enhance vortices and shear layers [7,8], promoting mixing between air and fuel, they may also cause particle deposition on the walls, leading to energy losses. In addition, extensive research has explored the effects of injector configurations [9–12] and the number of injectors [13,14] on combustion performance, revealing significant improvements in the mixing efficiency between the two jets. Active mixing enhancement methods based on external sources have also gained considerable attention. For instance, Shin et al. [15] utilized a plasma synthetic jet approach to induce bow shocks and oblique shocks in a supersonic flow field, resulting in noticeable deflection of the main flow. Ali et al. [16,17] investigated the use of multiple adjacent transverse jet injectors within the flow channel to induce oblique shocks. Their results demonstrated that this micro-jet array effectively enhances mixing and shear layer growth while reducing the flow losses caused by passive enhancement devices. Hiejima et al. [18] found that inducing oblique shocks downstream of struts facilitates the breakdown of large-scale vortex structures, leading to a maximum combustion efficiency improvement of 33%. Eri et al. [19] employed high-momentum synthetic jets to generate streamwise vortices and oscillations of the primary jet, significantly improving the mixing between subsonic jets and air. Overall, active mixing enhancement technology can promptly adjust to operational demands and offer lower total pressure losses compared to passive methods, which has high research potential.

In summary, active mixing enhancement technology represents an effective approach for improving the performance of solid rocket ramjets. However, the development and optimization of such technologies require reliable evaluation methods to quantitatively characterize the resulting changes in mixing and combustion organization. Therefore, establishing appropriate evaluation criteria is as important as developing new mixing-enhancement configurations. Existing evaluation methods for mixing and combustion organization in ramjet combustors can generally be classified into several categories. Flow-structure-based quantities, such as mixing-layer growth rate [20] and jet penetration [21], mainly characterize the macroscopic development of interacting jets. Scalar- or reaction-field-based quantities, including heat release rate [20], mixture fraction, flame index [22], scalar dissipation rate, and progress variables, are widely used to characterize reactant distribution, reaction-zone structure, and combustion progress in reacting flows. For particle-laden flows, the particle mixing degree [21,23–25] further considers the spatial relationship between particles and oxidizer, but mainly evaluates the degree of particle–oxidizer ratio matching. In addition, characteristic time-scale-based parameters, such as Damköhler and Karlovitz numbers, have been used to analyze the competition between reaction kinetics and transport processes and to identify the dominant combustion-control mechanisms of particles. Transport-topology-based approaches, such as FTLE methods, identify coherent structures and transport barriers that affect mixing evolution [26,27].

Collectively, these diagnostics provide complementary information on the mixing, reaction, transport, and combustion-control characteristics of reacting flows.

Nevertheless, these individual diagnostics focus on specific aspects of two-phase reacting flows and cannot directly characterize the overall combustion potential of particles under complex gas–solid reacting conditions. To address this issue, this study proposes a thermal-environment-informed particle combustion index based on particle oxidizer-consumption capacity. The proposed index integrates multiple combustion-related factors and provides a combustion-potential-oriented framework for evaluating particle-laden reacting flows.

In this work, the open-source CFD software OpenFOAM-13 is used to investigate the gas–solid reacting flow and mixing–combustion characteristics in a solid rocket ramjet afterburner. The remainder of this paper is organized as follows. Section 2 presents the numerical model, two-phase coupling algorithm, and formulation of the thermal-environment-informed particle combustion index. Section 3 assesses the proposed index using a reacting duct flow, a canonical jet-interaction flow, and a baseline solid rocket ramjet afterburner. Section 4 applies the index to pulsed-jet flow-control evaluation. Section 5 summarizes the main conclusions.

2. Numerical Model and Methodology

The numerical simulation of two-phase flow accompanied by a significant amount of partially combusted particles employs an Euler–Lagrange algorithm. The continuous phase was solved using OpenFOAM with the foamRun application and the multicomponentFluid solver. The gas mixture was described by the heRhoThermo thermophysical model, using a multicomponentMixture, Sutherland transport model, JANAF temperature-dependent thermodynamic data, sensible-enthalpy energy formulation, and perfect-gas equation of state. The particle phase was solved in the Lagrangian framework using the customized carbonCloud and boronCloud classes developed based on the reactingMultiphaseCloud class. The surface reaction rates of carbon and boron particles were calculated using the customized CarbonRate and BoronRate models developed from the SurfaceReactionModel class in ReactingMultiphase.

2.1. Continuous-Phase Governing Equation

The mass, momentum, and energy variations in the continuous phase are solved using the three-dimensional, transient, compressible Navier–Stokes (N-S) equations. The calculation considers mass and energy transport between the two phases, introduced in the form of source terms, and accounts for both gas–gas homogeneous reactions and gas–solid heterogeneous reactions among multiple components. The governing equations are presented as follows

$$\frac{\partial \rho}{\partial t} + \nabla \cdot \left(\rho \vec{U} \right) = S_m \tag{1}$$

$$\frac{\partial}{\partial t}\left(\rho \vec{U} \right) + \nabla \cdot \left(\rho \vec{U} \vec{U} \right) = -\nabla P + \nabla \cdot \tau + S_M \tag{2}$$

$$\frac{\partial}{\partial t}(\rho E) + \nabla \cdot \left[\vec{U}(\rho E + P) \right] = \nabla \cdot \left[\lambda \nabla T - \sum_i h_i \vec{J_i} + \left(\tau \cdot \vec{U} \right) \right] + S_E \tag{3}$$

$$\frac{\partial}{\partial t}(\rho Y_i) + \nabla \cdot \left(\rho Y_i \vec{U} \right) = -\nabla \cdot \vec{J_i} + R_i + S_i, (i = 1, 2, \ldots, N) \tag{4}$$

where ρ denotes the gas-phase density, P represents the pressure, and E is the total specific energy of the gas phase. t and $\vec{U}$ denote the time and velocity, respectively. S represents the source term, and the subscripts "m", "M", "E", and "i" represent the mass term, momentum

term, energy term, and species i, respectively. λ is the thermal conductivity. τ is the stress tensor. h_i, $\vec{J}_i$, and Y_i denote sensible enthalpy, diffusion flux, and mass fraction of species i. R_i is the chemical reaction rate for species i, and N represents the total number of species.

2.2. Discrete-Phase Governing Equations

The volume fraction of discrete phase is relatively low in fuel-rich gas, meeting the assumptions of the Discrete-Phase Model (DPM) for particle motion. Under this assumption, particle motion is described by the following equations

$$\frac{dx_p}{dt} = u_p \tag{5}$$

$$m_p \frac{du_p}{dt} = m_p \frac{18\mu}{\rho_p d_p^2} \frac{C_D Re}{24} (u_g - u_p) + m_p \frac{(\rho_p - \rho_g)}{\rho_p} g + F \tag{6}$$

where Re is the particle Reynolds number, g represents the gravitational acceleration. x_p is the particle position. m_p is the particle mass. F is the force exerted on the particle. u_g is the continuous-phase velocity. u_p is the particle velocity. μ is the continuous-phase dynamic viscosity. ρ_g is the continuous-phase density. ρ_p is the particle density. d_p is the particle diameter. C_D is the particle resistance coefficient.

2.3. Turbulence Model

The flow inside the solid rocket ramjet afterburner exhibits complex turbulent characteristics due to the interaction among the fuel-rich gas jet, incoming air stream, and transverse pulsed jets, including strong shear, jet interaction, flow separation, and recirculation regions. Reynolds-averaged Navier–Stokes (RANS)-based turbulence model frameworks have been widely employed for propulsion internal-flow simulations involving complex mixing, flow separation, and recirculation structures. Compared with the standard $k-\epsilon$ model, the Realizable $k-\epsilon$ model provides improved descriptions of such complex turbulent flows involving the aforementioned flow characteristics while maintaining reasonable computational efficiency for engineering-scale simulations [28]. Although higher-fidelity turbulence models, such as Reynolds Stress Models (RSM) and scale-resolving approaches, can provide more detailed descriptions of turbulence anisotropy and unsteady flow structures, the adopted model provides a reasonable compromise between accuracy and computational cost for the present engineering-scale analysis of particle combustion organization.

2.4. Combustion Model

2.4.1. Combustion Model of Continuous Phase

Based on previous research on ramjet combustion simulation [29], the Partially Stirred Reactor model (PaSR) is selected for gas-phase combustion. Table 1 summarizes the relevant gas-phase chemical reactions employed in the simulation.

$$CO + 1/2O_2 \rightarrow CO_2 \tag{7}$$

$$H_2 + 1/2O_2 \rightarrow H_2O \tag{8}$$

$$B_2O_2 + 1/2O_2 \rightarrow B_2O_3 \tag{9}$$

Table 1. The coefficient of each chemical reaction.

No.	A_k/[m^3·(kmol·s)$^{-1}$]	E_A/(J·kmol^{-1})	b	Ref.
(7)	3.48×10^8	8.4×10^7	2	[30]
(8)	3×10^{17}	0.0	−1	[30]
(9)	5×10^{12}	2×10^8	−2	[31]

2.4.2. Combustion Model of Discrete Phase

The discrete phase in the fuel-rich gas primarily consists of the combustible particle components boron (B) and carbon (C). The heterogeneous surface reactions of the particles were modeled in the Lagrangian particle framework. For carbon particles, the adopted carbon-combustion reaction pathways are listed in Equations (10)–(12). For boron particles, based on the comparative accuracy of existing boron-particle combustion models across the particle-size ranges typical of solid rocket ramjets, the PSU model [32,33] was selected to calculate the ignition and combustion states. The corresponding boron-ignition and boron-combustion reaction pathways are listed in Equations (13)–(21).

C combustion process (diameter is 10 μm):

$$C(s) + 1/2O_2 \rightarrow CO \tag{10}$$

$$C(s) + CO_2 \rightarrow 2CO \tag{11}$$

$$C(s) + H_2O \rightarrow CO + H_2 \tag{12}$$

B ignition process (diameter is 3 μm, oxide thickness is 0.02 μm):

$$B_2O_3(l) \rightarrow B_2O_3(g) \tag{13}$$

$$2/3B(s) + 2/3B_2O_3(l) \rightarrow B_2O_2 \tag{14}$$

$$B(s) + O_2 \rightarrow BO_2 \tag{15}$$

$$B(s) + 3/4O_2 \rightarrow 1/2B_2O_3 \tag{16}$$

$$2/3B(s) + 2/3B_2O_3(l) + H_2O + 1/2O_2 \rightarrow 2HBO_2 \tag{17}$$

$$B_2O_3(l) + H_2O \rightarrow 2HBO_2 \tag{18}$$

B combustion process:

$$2B(s) + O_2 \rightarrow B_2O_2 \tag{19}$$

$$2B(s) + 3/2O_2 + H_2O \rightarrow 2HBO_2 \tag{20}$$

$$B(l) \rightarrow B(Melting/Boiling) \tag{21}$$

2.5. Two-Phase Coupling Algorithm

The interaction between the continuous gas phase and the discrete particle phase was treated using a two-way coupling algorithm. The gas phase affects the particle trajectories and thermal states through drag and heat transfer, while the particles feed back to the gas phase through mass, momentum, energy, and species source terms. In each gas-phase time step, one Lagrangian parcel was injected from each inlet-face cell of the fuel-rich gas inlet to represent the physical particles entering with the fuel-rich gas. The particle phase was then advanced once synchronously with the gas phase within the same time step, and no additional inner particle–gas coupling iteration was imposed.

The interphase source terms were assembled from the particle increments within each computational cell during the time step. The mass consumed from the particles by surface reactions was converted into the corresponding gas-phase species source terms according to the reaction stoichiometry. The momentum exchange due to drag and the energy exchange due to heat transfer and heterogeneous reactions were added to the gas-phase governing equations with signs opposite to the corresponding particle-phase changes. Therefore, the particle–gas coupling is conservative at the discrete source-term level for the transferred mass, momentum, and energy.

2.6. Numerical Method Validation

To validate the accuracy of the numerical method, a direct-connect ignition experiment was conducted on a full-scale subsonic solid rocket ramjet to assess its suitability for gas–solid combustion simulation. The motor structure is shown in Figure 1, and the positions indicated by the arrow in the figure are the locations of the pressure sensors. The measurement points cover the head, middle, and tail sections of the afterburner, providing a comprehensive representation of the axial pressure variation. The wall pressure distribution was selected as the primary validation quantity because it provides an effective non-intrusive measurement of the integrated flow-field response, including the effects of mixing, expansion, and recirculation within the afterburner. In contrast, intrusive measurements of internal temperature, species concentration, or particle combustion characteristics may disturb the gas–solid flow organization and introduce additional uncertainties, particularly in particle-laden reacting flows. Therefore, the present validation focuses on assessing the accuracy of the overall flow-field prediction, while the particle combustion models are based on established heterogeneous combustion models reported in previous studies. Due to the motor's symmetric structure, a half-model was used in the calculations, with boundary conditions listed in Tables 2 and 3.

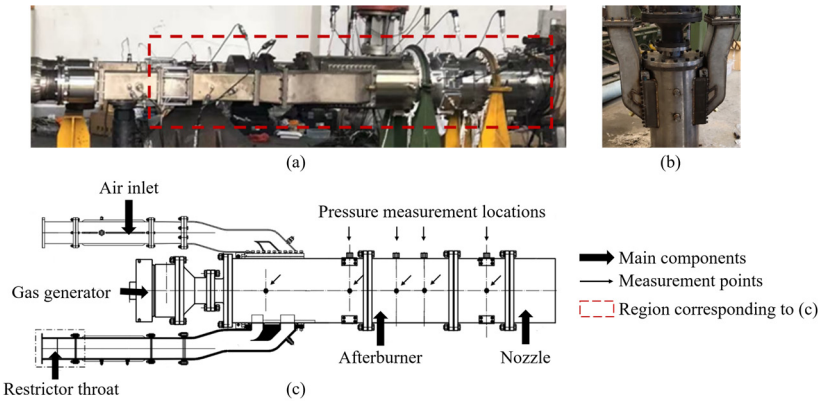


Figure 1. Schematic diagram of the direct-connect solid rocket ramjet configuration and pressure measurement locations: (**a**) photograph of the experimental setup; (**b**) photograph of the front section of the afterburner (with air inlets on both sides); (**c**) schematic drawing of the air inlets and afterburner (top view).

Table 2. Boundary conditions for gas–solid reaction.

Boundary	Mass Flow Rate, $\dot{m}$/(kg·s^{-1})	Temperature, T/K
Fuel inlet (Gas)	0.0144	1801.1
Air inlet	0.63	708.2

Table 3. Components of rich-fuel gas.

Component (Gas)	Mass Fraction	Component (Particle)	Mass Flow Rate, $\dot{m}$/(kg·s^{-1})
CO	0.432	B	0.0118
H_2	0.120	C	0.0081
$MgCl_2$	0.273	Al_2O_3	0.0020
N_2	0.175	B_2O_3	0.0037
		BN	0.0025

Using the pressure at the air inlet exit—where pressure variations are most pronounced—as comparative data, grid independence was verified with coarse, medium, and fine grid sizes, as shown in Figure 2. Results indicate that a 1.1 M cell count achieves the best balance between accuracy and computational cost. Using this grid, combustion simulation

was conducted, and differences in static pressure distributions along the upper and side walls between experimental and simulated results are shown in Figure 3. Near the inlet exit, two regions of steep pressure drop are observed, formed by merging jets, while in the downstream region, static pressure decreases gradually. The simulated wall pressure aligns well with the experimental result in both the head and downstream regions, with a maximum error of 2.05% across nine measurement points. This comparison indicates that the numerical method can reasonably reproduce the main characteristics of gas–solid reactive flows with intersecting jet interactions.

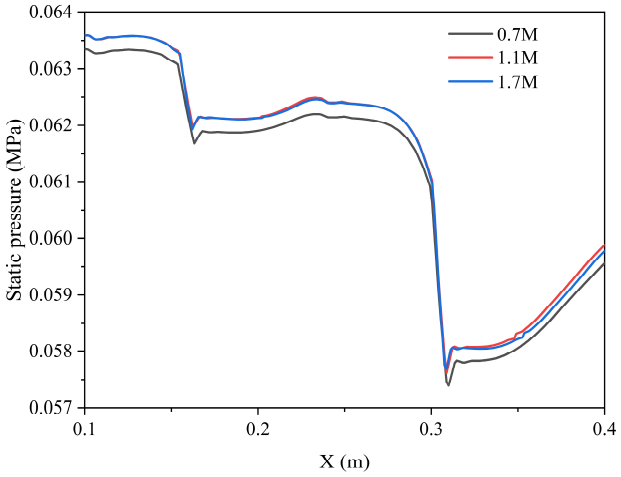


Figure 2. Grid independence verification at the side wall.

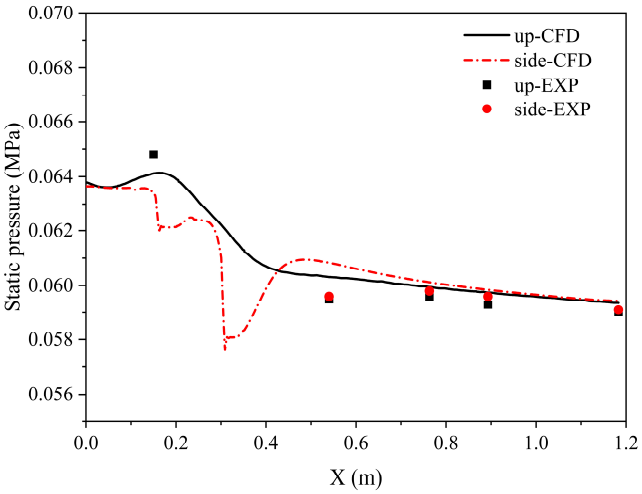


Figure 3. Static pressure distribution along axial wall surface.

2.7. Definition of the Thermal-Environment-Informed Particle Combustion Index

2.7.1. Conventional Particle Mixing Degree

For pure gas-phase reactions, the reaction rate is limited by the concentrations of both the oxidant and the fuel. Therefore, mainstream assessments of mixing degree in gas-phase combustion systems are based on the concentration ratio of the reactants. The commonly used evaluation of gas–solid mixing takes a similar approach, using the mass flow rate ratio of the two phases as a core parameter and considering the "premixed" state as the optimal mixing condition. For example, the definition of particle mixing degree [13,21,25] assumes that optimal mixing is achieved when the flow ratio of oxygen to particles in the region matches the initial ratio of these species upon entering the system. As the flow ratio

gradually deviates from this optimal point, the mixing degree correspondingly decreases until eventually approaching zero, as shown in Equation (22).

$$\beta_p = 1 - \frac{1}{1 + \lg\left[1 + \frac{\rho v Y_{O_2} n_p v_p m_p \eta_0}{\left(\rho v Y_{O_2} - n_p v_p m_p \eta_0\right)^2}\right]} \tag{22}$$

where β_p denotes the conventional particle mixing degree. $\rho v Y_{O_2}$ represents the product of gas-phase density, velocity, and oxygen mass fraction, indicating the oxygen flow through the mesh cell. $n_p v_p m_p$ represents the product of particle number density, particle velocity, and particle mass, indicating the particle-phase flow through the mesh cell. η_0 is the initial mass flow ratio of oxygen to particles when they enter the system.

2.7.2. Thermal-Environment-Informed Particle Combustion Index

This study proposes an evaluation method for combustion organization that focuses on the oxidant consumption capacity of high-energy particles. For this flow environment, the evaluation method should account for the following characteristics of particle-rich flow combustion: (1) the definition of mixing degree should not be influenced by the extent of reaction; (2) the thermal-environment of gas–solid reactions significantly impacts the local mixing and combustion state; (3) combustion in the afterburner occurs as surface reactions within a sparse particle flow, where the solid-phase mass involved in the reaction is much smaller than its total mass. The detailed derivation process is presented below.

The mass of oxidant and particles passing through a specific grid face per unit time is shown in Figure 4, where N_p represents the total number of particles passing through the face per unit time. The amount of particles reacting per unit time, Δm_P, can be expressed in the form of Equation (23).

$$\Delta m_P = m_{wP} \sum_{j=1}^{N_p} R_j A_{P-j} dt \tag{23}$$

where m_{wP} represents the molar mass of the particles. $R_j = k(T_{p-j}) P_{O_2}$, $k(T_p)$ denotes the reaction coefficient varying with particle temperature. A_{P-j} is the reactive surface area of the j-th particle. The oxidant consumption capacity of particles passing through a specific grid face per unit time can be characterized by Equation (24). η represents the stoichiometric ratio under complete reaction conditions.

$$\frac{\Delta m_{O_2}}{m_{O_2}} = \frac{\eta m_{wP} \left[\sum_{j=1}^{N_p} k(T_{p-j}) A_{P-j}\right] P_{O_2}}{\rho v A_{face} Y_{O_2}} \tag{24}$$

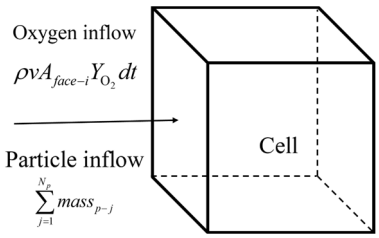


Figure 4. Mass of the reactants passing through the *i* face in unit time.

Based on the ideal gas law, the partial pressure of the oxidant in the system can be expressed as

$$P_{O_2} = P X_{O_2} = \rho R T X_{O_2} \tag{25}$$

$$R = \frac{R_0}{m_{wg}}, X_{O_2} = \frac{Y_{O2}/m_{wO_2}}{1/m_{wg}} \tag{26}$$

$$P_{O_2} = \rho \frac{R_0}{m_{wg}} T \frac{Y_{O_2}/m_{wO_2}}{1/m_{wg}} = \rho R_0 T Y_{O_2}/m_{wO_2} \tag{27}$$

Substituting Equation (27) into Equation (24) yields the following expression.

$$\begin{aligned} \frac{\Delta m_{O_2}}{m_{O_2}} &= \frac{\eta m_{wP} \left\{ \sum_{j=1}^{N_p} k(T_{p-j}) A_{P-j} \right\} \rho R_0 T Y_{O_2}/m_{wO_2}}{\rho v A_{face} Y_{O_2}} \\ &= \frac{\eta m_{wParticle} R_0 T \left[\sum_{j=1}^{N_p} k(T_{p-j}) A_{Particle-j} \right]}{m_{wO_2} v A_{face}} \end{aligned} \tag{28}$$

where Δm_{O_2} represents the mass consumed of oxidant by particle reactions, and m_{O_2} denotes the mass of oxidant passing through the considered region during the same time interval. A_{face} denotes the area of the computational face through which particles and oxidizer pass. m_{wO_2} represents the molar mass of oxidant, P_{O_2} represents the partial pressure of oxidant, X_{O_2} is the mole fraction of oxidant, R_0 denotes the universal gas constant.

According to the assumption that the definition of mixing degree should not be influenced by the extent of reaction, the variation in particle size should not affect the representation of mixing degree. Finally, the face-Field data used in the derivation process is reconstructed into the vol-Field format utilized by OpenFOAM for computation and storage. The total oxidant consumption capacity of all particles within a given region is then expressed as Equation (29).

$$\frac{\Delta m_{O_2}}{m_{O_2}} = f(T, v, N_p, T_p) \tag{29}$$

In engineering applications, researchers often aim to perform cross-comparisons of particle combustion performance under identical inflow conditions with different structures. This necessitates a unified reference point similar to η_0 in Equation (22). The following section introduces the methods for determining the reference values of the parameters in this study.

2.7.3. Factor Definitions and Reference Values

Based on Equations (28) and (29), the proposed index is constructed by converting the dominant variables in the oxidizer-consumption-capacity ratio into normalized monotonic factors. In Equation (28), the local gas temperature, the number density of reactive particles, and the particle-temperature-dependent reaction coefficient contribute positively to the oxidizer-consumption capacity of particles, whereas the gas velocity appears in the denominator and therefore reduces the relative oxidizer-consumption capacity through the residence-time effect. Accordingly, variables appearing in the numerator are mapped into monotonically increasing normalized factors, while the gas velocity is mapped into a monotonically decreasing velocity factor. This construction follows the algebraic structure of the oxidizer-consumption-capacity ratio rather than empirical weighting.

The core particle oxidizer-consumption capacity index is first defined as

$$F_p = F_T F_v F_n F_{T_p} \tag{30}$$

where F_T, F_v, F_n, and F_{T_p} represent the gas-temperature factor, gas-velocity factor, particle-number-density factor, and particle thermal-reactivity factor, respectively. The index F_p

describes the relative ability of particles to consume the local oxidizer under the local thermal and flow conditions.

However, a region with high F_p may still make a limited contribution to actual particle combustion if the local oxygen content is very low. Therefore, an additional oxidizer-availability factor F_Y is introduced to obtain the final thermal-environment-informed particle combustion index.

$$I_{TPCI} = F_Y F_p = F_Y F_T F_v F_n F_{T_p} \tag{31}$$

where I_{TPCI} is bounded within [0, 1]. A larger value of I_{TPCI} indicates that the local region is more favorable for effective particle combustion.

(1) Oxidizer-availability factor F_Y

The oxidizer-availability factor is defined as

$$F_Y = \min\left(\frac{Y_{O_2}}{Y_{O_2,ref}}, 1\right) \tag{32}$$

where Y_{O_2} is the local oxygen mass fraction and $Y_{O_2,ref}$ is the reference oxygen mass fraction. In the present study, $Y_{O_2,ref}$ is taken as the oxygen mass fraction at the air inlet.

(2) Gas-temperature factor F_T

The gas-temperature factor is defined as

$$F_T = \min\left(\frac{T}{T_{ref}}, 1\right) \tag{33}$$

Here, T is the local gas temperature and T_{ref} is the reference gas temperature. In this study, T_{ref} is determined from the adiabatic combustion temperature response with respect to the O/F ratio under a given nominal operating pressure.

$$T_{ref}(p_{op}) = \max_{\phi} T_{ad}(\phi, p_{op}) \tag{34}$$

where T_{ad} is the adiabatic combustion temperature, ϕ is the O/F ratio or equivalence-ratio-related parameter, and p_{op} is the nominal operating pressure of the afterburner. For comparisons among different configurations under the same operating condition, the same p_{op} and T_{ref} are used.

The reference pressure p_{op} should be selected as the nominal chamber pressure of the corresponding direct-connect test or design operating point. If such a nominal pressure is unavailable, it can be approximated by the spatially averaged pressure in the main reaction region of the baseline configuration. Once selected, the same p_{op} must be used for all configurations compared under the same operating condition to ensure consistency of the normalization.

(3) Gas-velocity factor F_v

The gas-velocity factor is defined as

$$F_v = \frac{v_c}{\max(v, v_c)} \tag{35}$$

where $v = |U|$ is the local gas velocity magnitude and v_c is the clipping velocity. The clipping velocity is defined as $v_c = 0.01 v_{in,\max}$ ($v_{in,\max}$ is the maximum inlet velocity among the air inlet and the fuel-rich gas inlet).

This factor represents the residence-time-related oxidizer-consumption capacity of particles. In low-speed recirculation regions, particles generally have longer residence time

and can consume a larger fraction of the oxidizer passing through the local region. In contrast, in high-speed oxygen-rich regions, the local oxidizer flux can be large, but the residence time of particles is shorter, which weakens the relative oxidizer-consumption capacity of particles.

(4) Particle-number-density factor F_n

To avoid interpreting the global decrease in particle number caused by reaction progress as a deterioration of local particle distribution, a reaction-progress-corrected reference particle number density is introduced. The surviving particle-number ratio at an axial location is defined as

$$\chi_N(x) = \frac{\dot{N}_{p,cross}(x)}{\dot{N}_{p,in}} \tag{36}$$

where $\dot{N}_{p,in}$ is the particle number flux at the fuel-rich gas inlet and $\dot{N}_{p,cross}(x)$ is the particle number flux passing through the axial section at χ. The corrected reference particle number density is then written as

$$N^*_{p,ref}(x) = \chi_N(x) n_{p,ref,0} \tag{37}$$

where $n_{p,ref,0}$ is the reference particle number density at the fuel-rich gas inlet. The particle-number factor is defined as

$$F_n = \min\left(\frac{n_p}{N^*_{p,ref}(x)}, 1\right) \tag{38}$$

n_p is the local particle number density. This treatment makes F_n mainly reflect local particle enrichment or dilution relative to the remaining particle population, rather than the overall decrease in particle number caused by particle consumption. Therefore, the particle-number factor is less affected by the reaction progress while retaining the effect of local particle accumulation.

(5) Particle thermal-reactivity factor F_{T_p}

The particle thermal-reactivity factor is introduced to describe whether the particles have reached a thermal state favorable for heterogeneous combustion. To make this factor applicable to different particle-combustion models, it is not restricted to a specific Arrhenius-type coefficient. Instead, it is defined through a model-dependent normalized thermal activation function:

$$F_{T_p} = \frac{1}{N_p}\sum_{j=1}^{N_p} \Theta_p(T_{p,j}) \tag{39}$$

$$\Theta_p(T_p) = \min\left(\frac{\kappa_p(T_p)}{\kappa_p\left(T_{p,ref}\right)}, 1\right) \tag{40}$$

$\kappa_p(T_p)$ denotes the model-dependent thermal activation function of particle combustion. If the adopted particle-combustion model provides a temperature-dependent kinetic coefficient, κ_p is taken as that coefficient. If the model uses a temperature-independent coefficient but includes an ignition or activation threshold, κ_p is represented by a normalized transition function between T_{ign} and $T_{p,ref}$. If the model contains no explicit particle-temperature limitation, F_{T_p} is set to unity. In the present study, F_{T_p} is simplified as a constant for carbon combustion, whereas for boron combustion it is approximated by a linear variation between the ignition temperature and the melting point.

(6) Interpretation of the multiplicative formulation

The proposed index does not introduce empirical weighting coefficients. The multiplicative form does not assume statistical independence among the factors. Instead, it repre-

sents a limiting-condition formulation derived from the normalized oxidizer-consumption-capacity ratio. For strong local particle combustion, several necessary conditions must be satisfied simultaneously: sufficient oxidizer availability, favorable gas thermal environment, adequate particle residence time, local enrichment of reactive particles, and sufficiently high particle temperature. If any one of these conditions is absent, the corresponding factor approaches zero, and the final index decreases accordingly. Therefore, the multiplicative formulation should be understood as a physical limiting-condition model rather than an equal-weight linear combination. The role of each factor can be further examined through factor-ablation analysis in the baseline afterburner case, where the full index is compared with the index obtained after removing individual factors. This analysis is used only to diagnose the contribution of each factor to the spatial distribution of the index, not to establish statistical independence among the factors. The definitions and physical meanings of the normalized factors are summarized in Table 4.

Table 4. Definitions and physical meanings of the normalized factors.

Factor	Physical Meaning	Reference Value
F_Y	Local oxidizer availability	Oxygen mass fraction at air inlet
F_T	Gas thermal environment for particle ignition and combustion	Peak adiabatic combustion temperature from the O/F ratio response at p_{op}
F_v	Residence-time-related oxidizer-consumption capacity	$v_c = 0.01 v_{in,\max}$
F_n	Local enrichment of reactive particles	Particle number density at the fuel-rich gas inlet
F_{T_p}	Particle-temperature-controlled heterogeneous reactivity	Characteristic particle temperature, e.g., boron melting point

3. Assessment of the Proposed Index

The following simplified configurations are not intended to provide a comprehensive validation of I_{TPCI} against all existing combustion diagnostics. Instead, they are designed to isolate specific physical factors affecting particle combustion organization and to demonstrate how I_{TPCI} interprets these effects compared with the conventional particle mixing degree.

3.1. Comparison in a Reacting Duct Flow

Conventional particle mixing degree evaluates mixing quality solely based on the deviation of the local reactant-flow ratio from a prescribed optimal mixing point. This treatment cannot distinguish particle depletion caused by combustion from particle deficiency caused by poor mixing. To illustrate this limitation, an idealized horizontal duct is considered, as shown in Figure 5. The flow-rate ratio used here is normalized by the stoichiometric oxidizer demand of the particle reaction. Specifically, if the stoichiometric oxidizer-to-particle mass ratio is denoted by s, the normalized oxidizer flow rate is defined as the actual oxidizer flow rate divided by s, while the particle flow rate is normalized by its own mass flow rate. Therefore, a normalized ratio of 1:1 represents the stoichiometric reaction condition, rather than an equal physical mass flow rate of oxidizer and particles.

Based on this normalization, oxygen and particles are assumed to enter the duct uniformly with a normalized initial flow-rate ratio of 1.5:1, indicating that the available oxidizer is 50% higher than the stoichiometric demand of the incoming particles. The normalized reaction-consumption ratio is then 1:1 by definition. After a certain reaction distance, if half of the particles are consumed by oxidation, half of the stoichiometrically equivalent oxidizer is also consumed. Consequently, the remaining normalized oxidizer and particle flow rates

become 1.0 and 0.5, respectively. According to Equation (22), the particle mixing degree is unity at the duct inlet but decreases downstream, although the reduction in particle loading is caused by reaction rather than by deteriorated mixing. Therefore, the conventional index may interpret a progressive reacting process as a reduction in mixing quality.

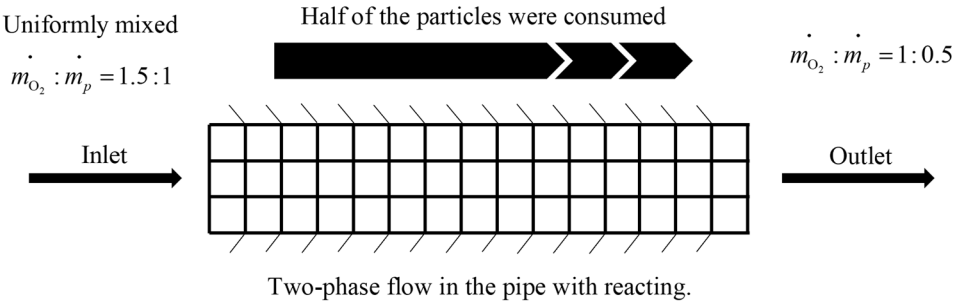


Figure 5. The diagram of reacting duct flow.

To investigate this type of reacting duct-flow problem, a canonical reacting case is constructed in a straight circular duct with a length of 1 m and a diameter of 0.2 m, where carbon particles react with air according to $C + O_2 \rightarrow CO_2$. The purpose of this case is to examine how particle consumption during combustion affects the evaluation of mixing. The computational conditions are summarized in Table 5, and the stoichiometric oxidizer-to-particle mass ratio is specified as 1:0.08625.

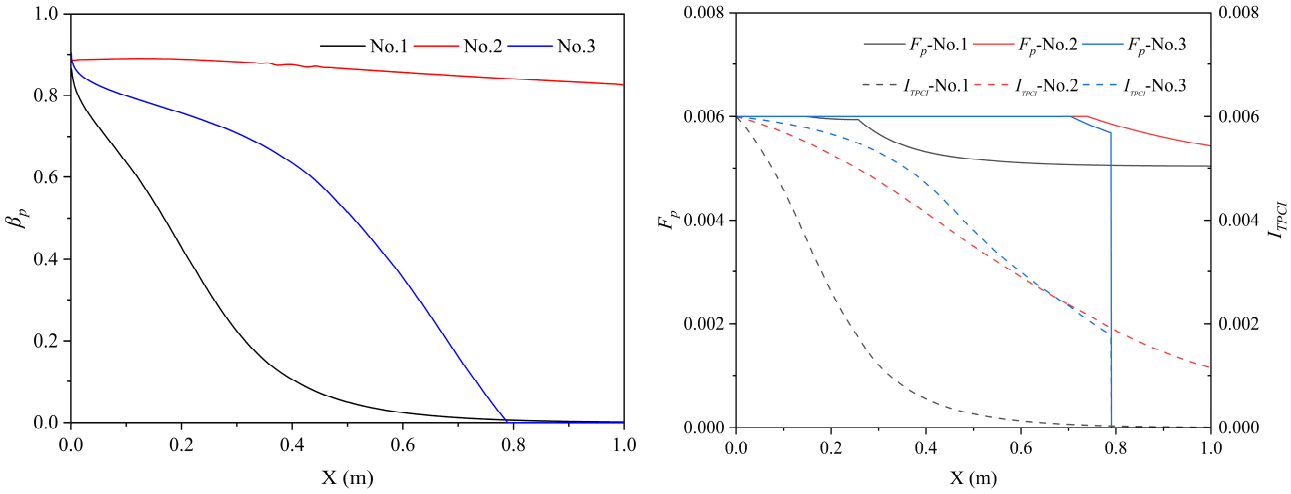
Table 5. Computational conditions of the reacting duct flow cases.

No.	Normalized Mass Ratio	Mass Flow Rate/(kg·s^{-1})		Static Temperature/(K)
		Air	C (10 μm)	
1	0.5:1	0.5	0.08625	1801.1
2	1:1	1.0		
3	1.5:1	1.5		

The $C + O_2 \rightarrow CO_2$ reaction is described using a diffusion/kinetics-controlled surface-reaction model. In this simplified reacting-duct case, the kinetic parameters in the reaction-rate expression are prescribed as constants. Therefore, the temperature-dependent kinetic correction factor F_{T_p} is not considered. The axial distributions of the conventional particle mixing degree and the proposed particle combustion index are shown in Figure 6. For the three inlet conditions listed in Table 5, the corresponding inlet velocities are 81.562, 163.124, and 244.686 m/s for Cases No. 1, No. 2, and No. 3, respectively. The corresponding particle burnout fractions are 49.85%, 77.18%, and 100%.

As shown in Figure 6a, the conventional particle mixing degree exhibits markedly different axial behaviors under the three normalized reactant-flow ratios. For Case No. 2, where the inlet condition is close to the stoichiometric reference ratio, the particle mixing degree remains at a relatively high level along most of the duct. This is because the consumption of oxidizer and particles proceeds approximately according to the prescribed optimal proportion, so that the local reactant-flow ratio does not deviate strongly from the reference mixing point. In contrast, for Case No. 1, the particle mixing degree also decreases along the duct, but the decrease is associated with insufficient oxidizer supply and incomplete particle consumption. These results demonstrate that the conventional mixing degree cannot distinguish between reaction-induced particle depletion and genuine mixing deficiency. For Case No. 3, the particle mixing degree decreases rapidly in the upstream part of the duct and approaches zero downstream. This decrease does not indicate that the inlet reactants become less uniformly mixed; rather, it is mainly caused by the rapid consumption of particles under an oxidizer-rich

condition. Therefore, the conventional index interprets the reduction in the remaining particle loading as a deterioration of particle mixing.



(**a**) Particle mixing degree (**b**) Particle combustion index

Figure 6. Axial evolution of particle mixing and combustion characteristics in the reacting duct flow.

Figure 6b further compares the axial variations in the factor F_p and the particle combustion index I_{TPCI}. For F_p, all three cases exhibit a similar trend: the curve first remains nearly flat and then decreases gradually downstream. However, clear differences can be observed among the three operating conditions. In Case No. 1, which corresponds to the oxidizer-lean condition, the plateau of F_p persists over a much shorter axial distance than those in the other two cases. This indicates that, under insufficient oxidizer supply, the heat release induced by particle combustion and the gas expansion/acceleration cannot maintain a dynamic balance, and the effective oxygen-consumption capability of the particles is relatively weak. Compared with the conventional particle mixing degree, I_{TPCI} provides an intensity ranking that is more consistent with the particle burnout fraction. Although the I_{TPCI} of Case No. 3 is only 13.76% higher than that of Case No. 2, Case No. 3 corresponds to a 50% larger oxidizer flow rate. Therefore, the slightly higher I_{TPCI} should not be regarded as a marginal improvement only. Instead, it indicates that the particle-combustion organization can be maintained at a higher level even under a larger-throughput condition.

Overall, the reacting duct-flow case confirms the theoretical analysis illustrated in Figure 5. The conventional particle mixing degree is suitable for evaluating the spatial uniformity of a passive particle scalar, but it is insufficient for assessing a reacting particle-laden flow. Once particle consumption is involved, a decrease in particle mixing degree may either indicate poor reactant supply or effective combustion, and these two mechanisms cannot be distinguished by the conventional index. By contrast, the proposed particle combustion index evaluates the particle phase in relation to the local oxidizer availability and reaction progress. This reacting duct flow case provides a process-resolved comparison between the two indices, and the relative magnitude of the particle combustion index corresponds to the overall particle burnout fraction. A more complex canonical jet-interaction flow is further examined in the following section to evaluate whether the proposed index can identify combustion-organization differences in a multidimensional mixing field.

3.2. Comparison in a Canonical Jet-Interaction Flow

The mixing and combustion characteristics of interacting jets are investigated using a rectangular mixing chamber with two jets, as shown in Figure 7. Referring to the computa-

tional model in Ref. [34], the total length L of the computational domain is 220 mm, while height H are 60 mm. The width H_1 of the fuel inlet is 3 mm with an installation height h of 50% H, and the width H_2 of the air inlet is 12 mm with a horizontal position l of 60% H. The calculations are performed using a two-dimensional model; the boundary conditions used in the calculation are listed in Table 6.

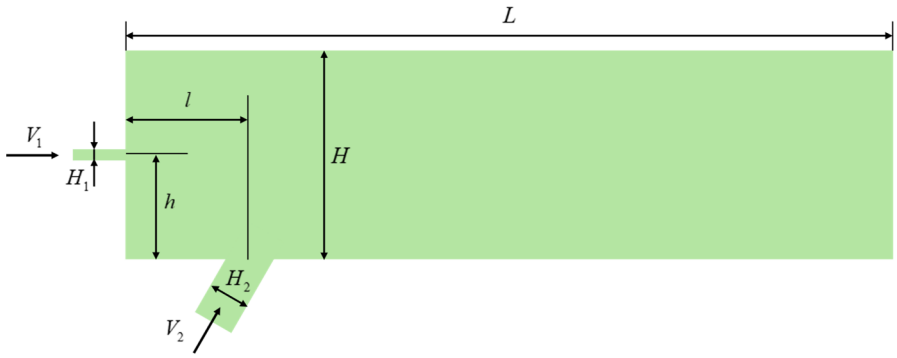


Figure 7. Definition of the computational domain of canonical jet-interaction flow.

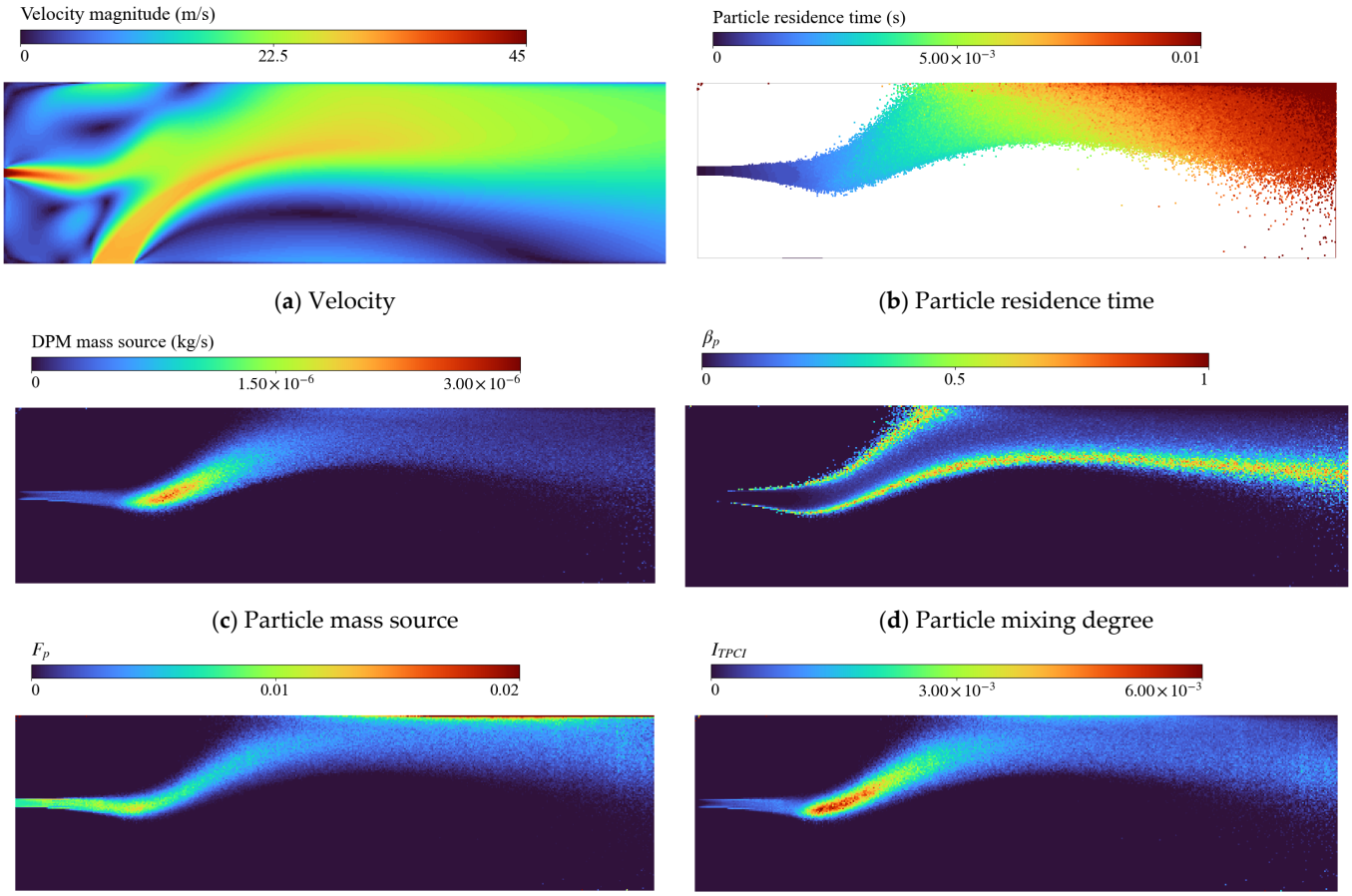
Table 6. Test case definitions.

Boundary	Mass Flow Rate/(kg·s^{-1})	Velocity/(m·s^{-1})	Static Temperature/(K)	Component
Air	0.1786	30	708.2	$0.23O_2 + 0.77N_2$
Fuel	Gas: 0.027 Particle: 0.0411	45 45	1801.1 1801.1	$0.3CO_2 + 0.1H_2O + 0.6N_2$ C

Figure 8 illustrates the spatial correspondence among the two-phase flow structure, particle consumption, and different evaluation quantities in the canonical jet-interaction flow. The transverse air jet strongly deflects the particle-laden fuel stream and generates a pronounced shear-dominated interaction region, in which the particle plume is rapidly bent and subsequently expands downstream. The particle residence time increases along the streamwise direction, whereas the particle mass source is mainly concentrated in the near-field interaction region, where particles, oxidizer, and a favorable thermal environment coexist. The downstream attenuation of the mass source should not be interpreted as the cessation of particle consumption; instead, it reflects the reduction in local reaction intensity as the particle plume is diluted and partially consumed. The conventional particle mixing degree β_p forms two elongated high-value bands along the deflected plume, indicating that it mainly responds to the interfacial transport barrier between the particle-laden stream and the oxidizer-rich surrounding flow. In this jet-interaction flow, such barriers correspond to the shear layers on both sides of the particle plume. By comparison, F_p and I_{TPCI} describe the local reaction potential of the particle phase under the prevailing thermochemical environment. Their distributions therefore emphasize regions with favorable particle oxidizer-consumption capability rather than the shear-layer interfaces identified by β_p.

Figure 9 further compares the heightwise distributions of the particle mass source and different evaluation quantities at selected axial locations. The particle mass source generally exhibits a single dominant peak, indicating that the intense particle-consumption region is concentrated within a limited portion of the deflected particle plume. By contrast, the conventional particle mixing degree β_p presents a distinct double-peak structure. According to its definition, β_p evaluates the closeness between the local two-phase mass ratio and the initial particle-to-oxidizer mass ratio; thus, its high values require both particles and oxidizer to be locally available. In the present jet-interaction flow, this condition is mainly satisfied near the two sides of the particle plume, where shear-layer-dominated transport barriers

separate the particle-laden stream from the oxidizer-rich surrounding flow. Therefore, the two peaks of β_p represent the two interfacial regions where the local two-phase ratio approaches the initial feeding ratio, rather than two regions of strong particle consumption. For surface-controlled heterogeneous particle combustion, the local oxidizer-consumption capability is not equivalent to the local equivalence-ratio-like mixing state, because the particle reaction rate is much slower than that of gas-phase homogeneous reactions. As a result, the particle mass source and the reaction-potential-oriented quantities tend to show a single-peak distribution. The closer correspondence of F_p and I_{TPCI} with this single-peak behavior indicates that they characterize the local particle reaction potential under the thermochemical environment, whereas β_p primarily identifies the locations where the two-phase mixing ratio becomes favorable from a transport perspective.



(**a**) Velocity (**b**) Particle residence time

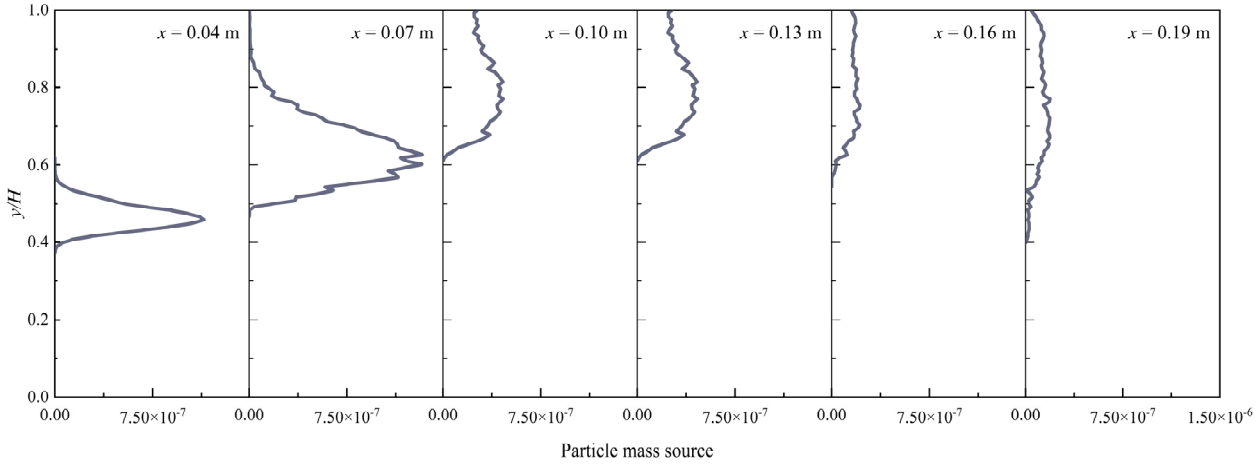
(**c**) Particle mass source (**d**) Particle mixing degree

(**e**) Particle oxidizer-consumption capacity index (**f**) Thermal-environment-informed particle combustion index

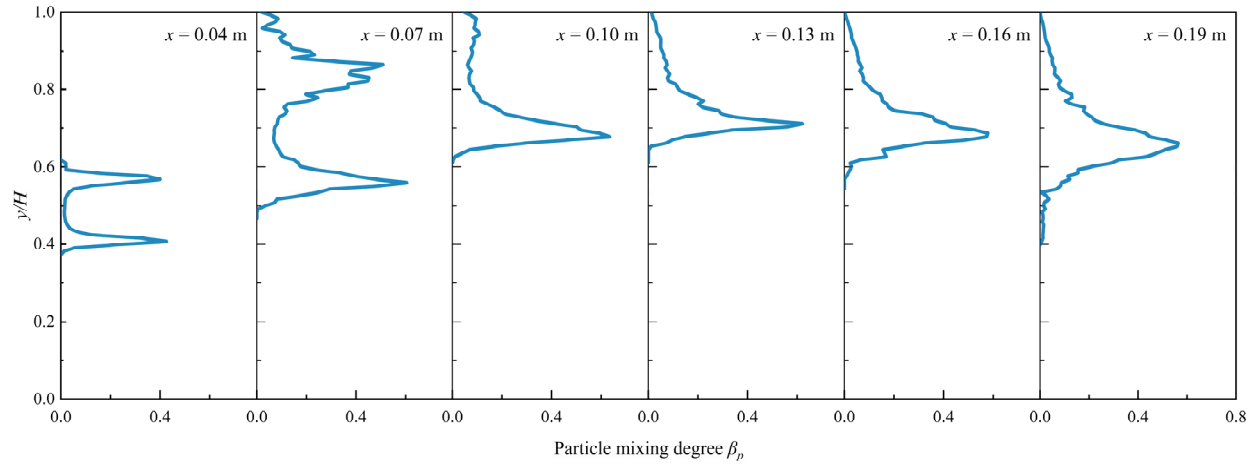
Figure 8. Distributions of two-phase parameters.

Overall, the canonical jet-interaction case highlights the different physical meanings of the conventional particle mixing degree and the proposed reaction-potential-oriented quantities. The conventional β_p is effective in identifying regions where the local particle-to-oxidizer ratio approaches the initial feeding ratio, which correspond to the shear-layer-dominated transport interfaces on both sides of the deflected particle plume. However, these interfacial regions do not necessarily coincide with the region of strongest particle consumption, because surface-controlled heterogeneous particle reactions are limited by local thermochemical conditions and finite reaction rates. In comparison, F_p and I_{TPCI} are more directly associated with the local oxidizer-consumption capability of the particle phase. The comparison therefore suggests that the proposed index provides a more combustion-relevant description of particle behavior in jet-interaction flows, while the

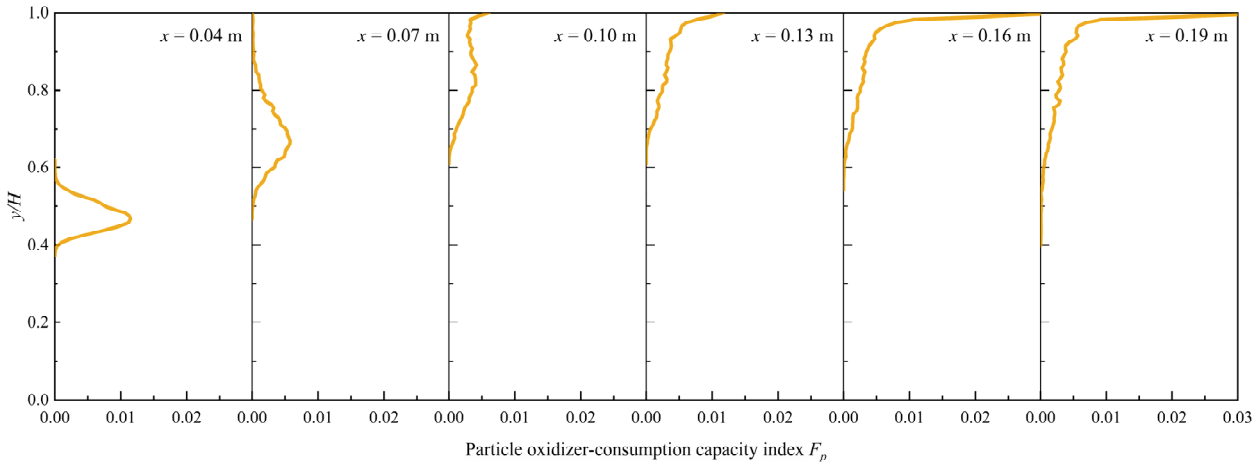
conventional mixing degree remains useful for characterizing two-phase transport and mixing interfaces.



(**a**) Particle mass source



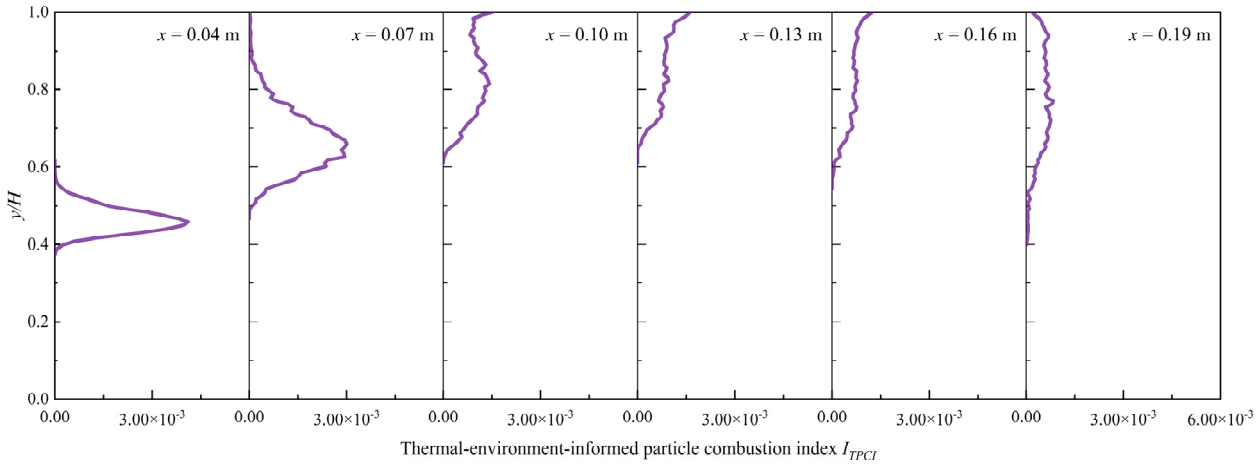
(**b**) Particle mixing degree



(**c**) Particle oxidizer-consumption capacity index

Figure 9. *Cont.*

https://doi.org/10.3390/aerospace13080697



(**d**) Thermal-environment-informed particle combustion index

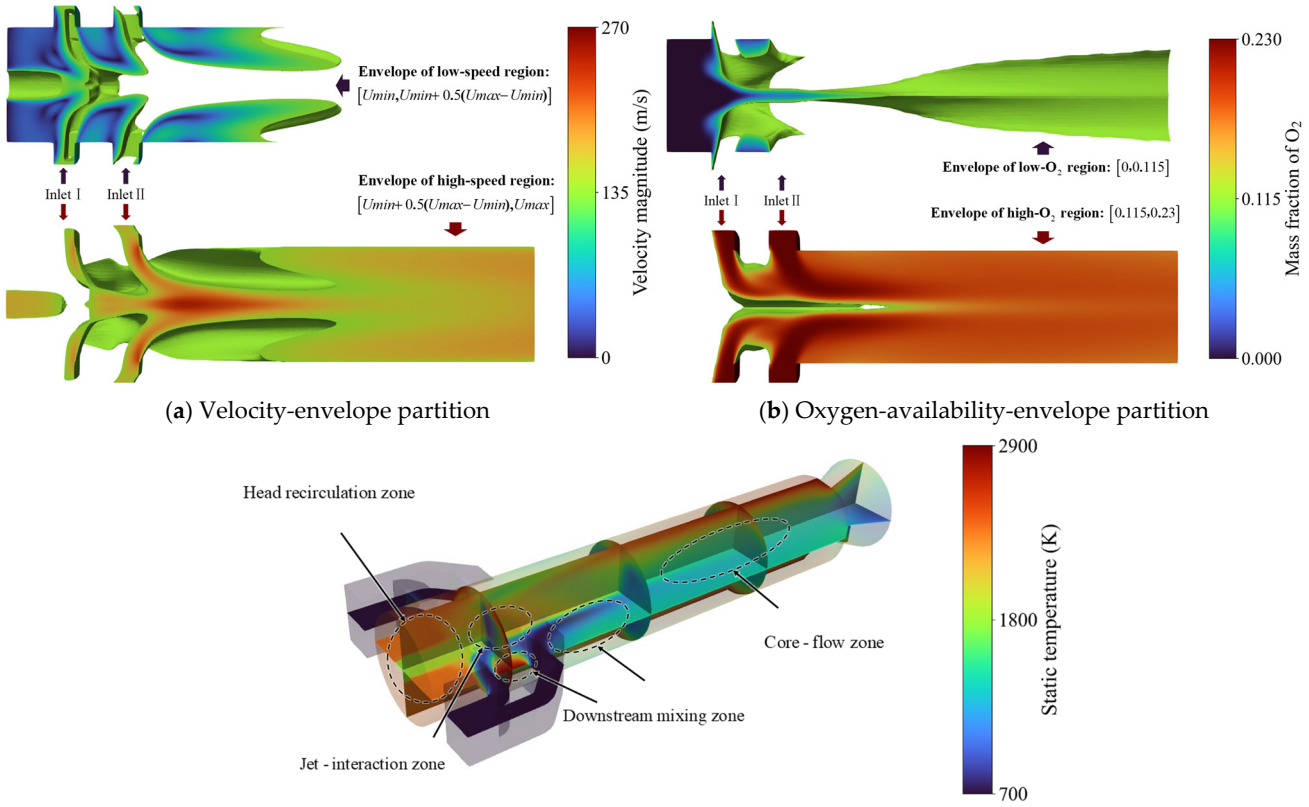
Figure 9. Heightwise comparison between the actual particle mass source and different particle-combustion evaluation quantities at selected axial locations.

3.3. Application to the Baseline Solid Rocket Ramjet Afterburner

In the preceding simplified cases, the proposed evaluation index has demonstrated its capability to identify particle combustion potential in both reacting duct flow and canonical jet-interaction configurations. To further examine the behavior of the proposed index in a realistic afterburner flow organization, the index is applied here to the baseline solid rocket ramjet afterburner. The computational model, operating condition, and boundary conditions are consistent with those described in Section 2.6. Therefore, this section does not repeat the numerical details, but focuses on the flow organization, oxygen distribution, thermal environment, and their effects on the evaluation of particle combustion potential in the baseline configuration.

Compared with the simplified cases discussed above, the practical afterburner involves several coupled processes, including head recirculation, staged lateral air injection, oxygen replenishment, main-flow acceleration, and particle-phase transport. The particle combustion potential is therefore not determined by the particle oxygen mixing degree or the local oxygen concentration alone. Instead, it is jointly constrained by the oxygen particle transport condition, the local residence condition, and the maturity of the thermal environment. Before analyzing the evaluation indices, it is necessary to first identify the major flow and oxidizer distribution characteristics in the baseline afterburner.

Figure 10 presents the flow organization characteristics of the baseline afterburner based on the velocity field, oxygen distribution, and temperature field. Figure 10a shows the spatial distribution of the high-speed transport region and the low-speed residence or recirculation region through the velocity envelope. Figure 10b reveals the organization of oxidizer availability by staged lateral air injection through the oxygen availability envelope. Figure 10c further provides a temperature-based synthesis map to show the thermal environment associated with different flow and oxygen-supply regions. The comparison among these distributions indicates that regions favorable for particle oxygen encounter do not necessarily possess a thermal environment suitable for rapid particle reaction. Similarly, regions with relatively high temperature may still be limited by insufficient oxygen supply, particle transport, or residence time. The baseline afterburner is therefore a representative configuration for examining the thermal-environment-constrained evaluation method proposed in this study.



(**a**) Velocity-envelope partition (**b**) Oxygen-availability-envelope partition

(**c**) Temperature-based synthesis map of the baseline afterburner

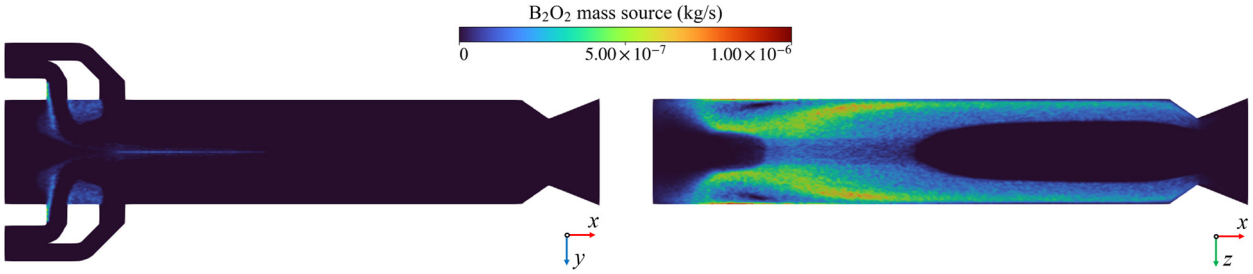
Figure 10. Flow and oxidizer-distribution-based zoning of the baseline afterburner.

As shown in Figure 10a, the velocity field in the baseline afterburner exhibits pronounced spatial nonuniformity. Several low-speed regions are formed near the head end and the lateral air inlets. These regions are usually associated with recirculation, leeward zones of the air jets, or local stagnation structures. The presence of low-speed regions can increase the particle residence time, but whether this residence advantage can be converted into effective particle combustion potential still depends on the local oxygen supply and thermal environment. In contrast, the downstream main-flow region exhibits a stronger high-speed transport feature, indicating that the flow gradually changes from jet interaction-dominated behavior to main-flow development. The high-speed region promotes the axial transport of particles and gas-phase species, but excessive velocity may also reduce the local residence time available for reaction. Therefore, the velocity field alone is insufficient for determining whether particle combustion is favorable. Figure 10b further shows the oxygen availability envelope. Owing to the staged lateral air injection, the oxygen-rich regions are mainly controlled by jet penetration, entrainment, and downstream diffusion from each air inlet. The oxygen distribution does not fully coincide with the velocity envelope. Some oxygen-rich regions are located in jet interaction and enhanced shear regions, whereas some low-speed or recirculation regions do not necessarily have sufficient oxygen replenishment. This indicates that conventional criteria based on two-phase mixing or local species ratio can identify possible particle oxygen encounter regions, but they cannot distinguish whether these regions satisfy the thermal condition required for effective reaction. Figure 10c presents the temperature-based synthesis map. Compared with the velocity and oxygen availability envelopes, the temperature distribution more directly reflects the thermal environment required for particle reaction. Although lateral air injection can enhance local oxygen supply and shear mixing, it may also introduce relatively low-temperature gas, causing some oxygen-rich regions to be inconsistent with

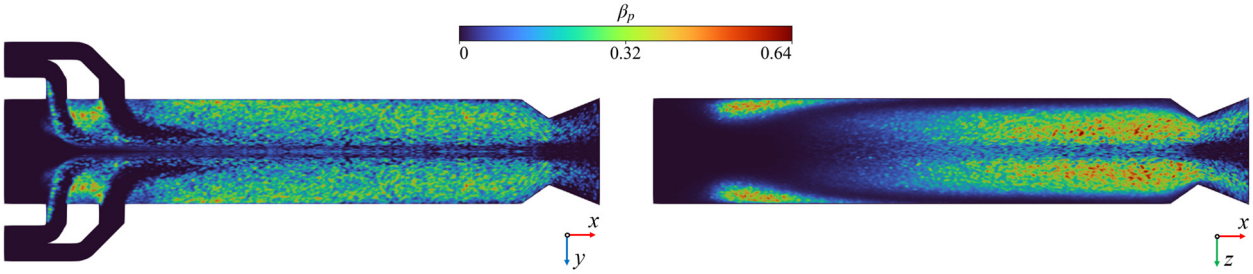
high reaction potential regions. In the downstream main-flow region, mixing and thermal diffusion have developed to some extent, but the particle combustion potential is still jointly affected by oxygen availability, particle residence time, and particle thermal state. Therefore, the velocity, oxygen, and temperature distributions exhibit clear spatial mismatch. This mismatch explains why a single mixing index is insufficient to fully characterize the particle combustion state.

Based on the nonuniformity of flow organization, oxygen supply, and thermal environment described above, the spatial distributions of the particle reaction source term, the conventional particle mixing degree, and the proposed evaluation indices in the baseline afterburner are further compared. Figure 11 compares the spatial distributions of the particle reaction source term, the conventional particle mixing degree, and the proposed evaluation indices in the baseline afterburner. It should be noted that the B_2O_2 mass source represents the actual reaction intensity in the current flow field, whereas β_p, F_p, and I_{TPCI} correspond to different physical evaluation objectives. Specifically, β_p describes the degree to which the local oxygen flow and particle flow ratio approaches the initial mass ratio. F_p describes the relative ability of particles to consume oxidizer under the local thermal and flow conditions. I_{TPCI} further introduces the oxidizer availability constraint into F_p. Therefore, these evaluation quantities should not be interpreted as point-by-point predictions of the reaction source term. Instead, they should be compared in terms of their ability to identify potentially favorable reaction regions, exclude regions with insufficient oxygen or unfavorable thermal and flow conditions, and reveal the limiting mechanisms of particle combustion organization. To prevent local stagnation points or extreme values from dominating the contour visualization, the relevant variables are displayed using global percentile-based color scales. Values above the upper color limit are retained and shown as saturated regions.

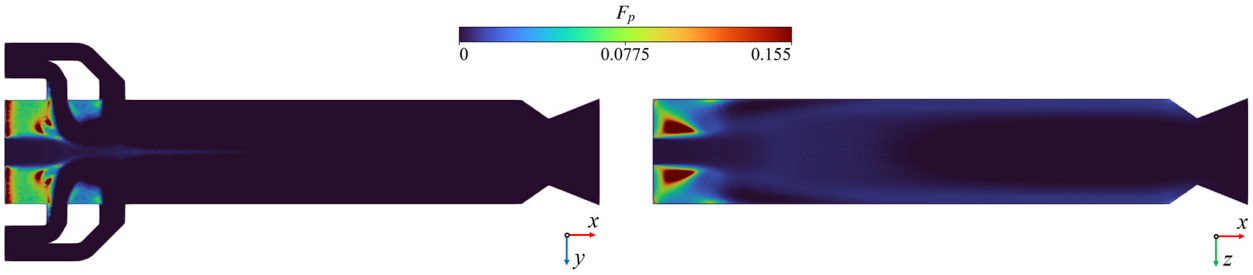
As shown in Figure 11a, the B_2O_2 mass source is mainly concentrated in regions where local shear, recirculation, and oxygen replenishment act together. This indicates that particle reaction does not simply increase with the spreading range of the particle cloud, but depends on the local coupling among particles, oxygen, residence time, and the thermal environment. Some downstream regions still have certain particle transport and oxygen replenishment conditions, but their actual reaction source term is not necessarily significant because of insufficient local thermal environment, particle thermal state, or residence condition. The conventional particle mixing degree in Figure 11b mainly reflects the degree to which the local oxygen flow and particle flow ratio approaches the initial mass ratio. Its high-value regions usually appear where strong shear and transport occur between the particle jet and the oxygen-containing main flow. Therefore, β_p can identify the transport-boundary and ratio-matching regions between particles and oxidizer. However, β_p does not include thermal-environment information such as local temperature and particle thermal state. As a result, its high-value regions do not necessarily correspond to regions with high actual reaction intensity. In particular, in regions where oxygen and particles coexist but the thermal environment is insufficient, the conventional particle mixing degree may still give a high evaluation, which may result in a high mixing evaluation despite a limited combustion potential under the local reaction conditions.



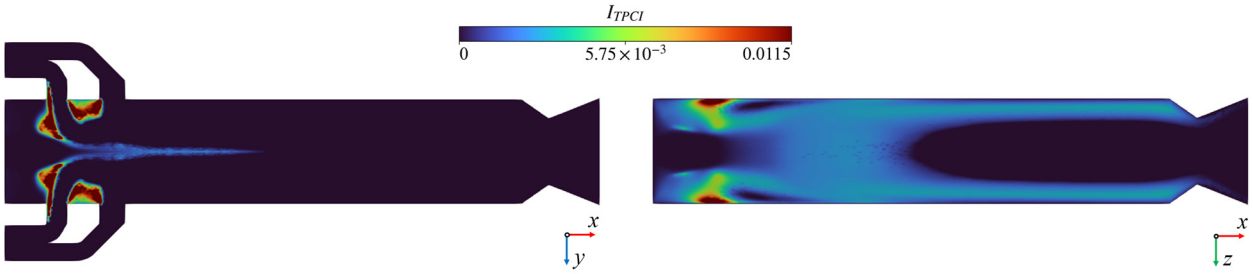
(**a**) B_2O_2 mass source



(**b**) β_p



(**c**) F_p



(**d**) I_{TPCI}

Figure 11. Spatial comparison of particle combustion source and evaluation indices in the baseline afterburner. The left and right panels show the *xy* and *xz* planes, respectively. Color scale for F_p: 0 to P99(F_p), color scale for I_{TPCI}: 0 to P99(I_{TPCI}). All panels use global percentile limits; values above the upper limit are shown with saturated color.

Different from the ratio-matching objective of β_p, F_p in Figure 11c evaluates the potential ability of particles to participate in oxidation reactions from the perspective of their relative oxidizer consumption capacity. Since F_p consists of the gas-temperature factor, gas-velocity factor, particle-number-density factor, and particle-thermal-reactivity factor, its high-value regions do not simply correspond to regions where particles and oxygen overlap most strongly. Instead, they tend to appear where particles have relatively strong reactivity, and the local flow condition is favorable for oxidizer consumption. The

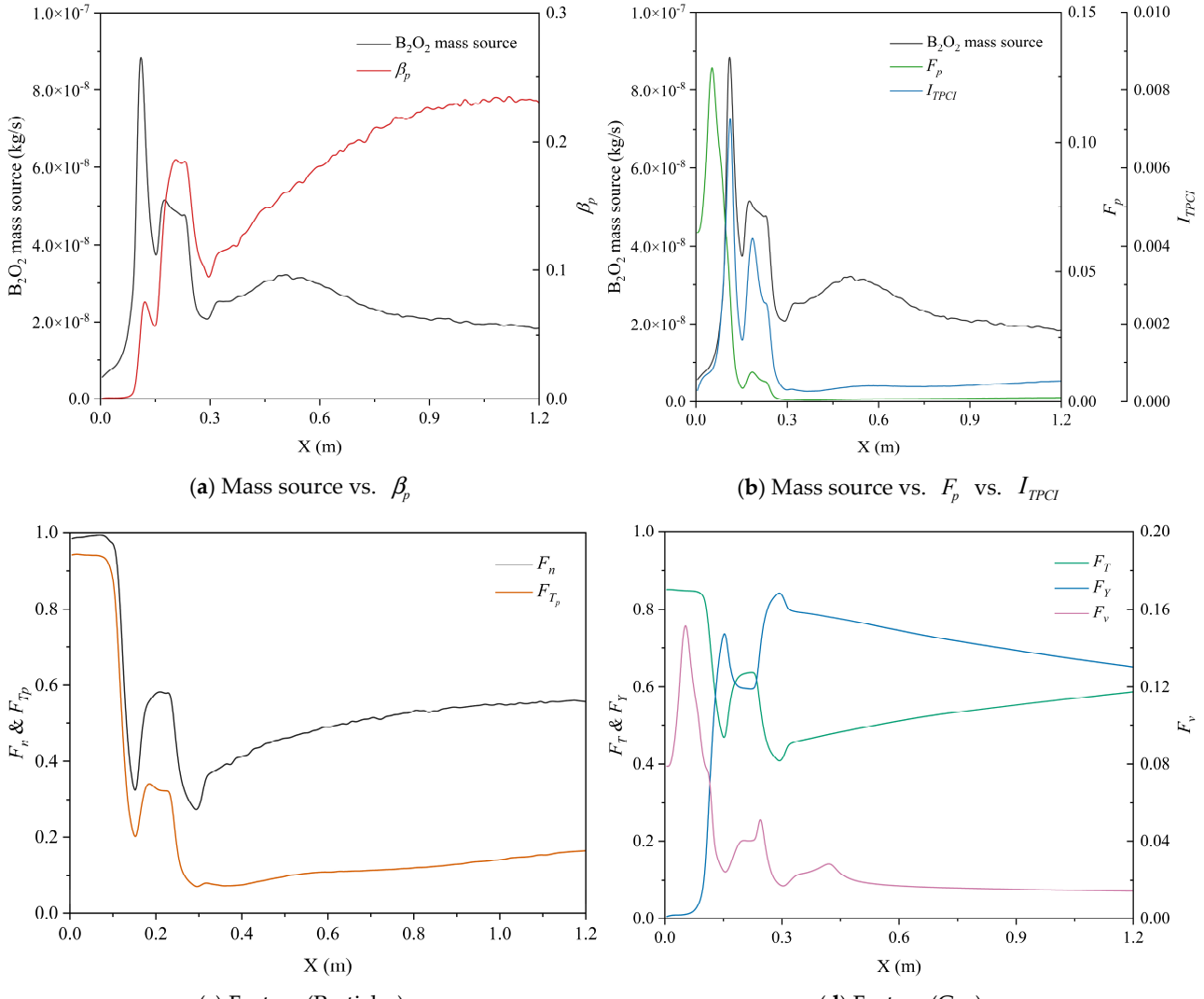
contours show that the high-value regions of F_p are mostly concentrated in the head recirculation region and its neighboring area. This indicates that this region has the strongest particle combustion potential within the present evaluation framework under the combined effects of local residence, particle accumulation, and thermal environment. In contrast, although some downstream regions have particle transport and a certain degree of oxygen replenishment, the response of F_p is significantly weakened. This suggests that local encounter or ratio matching cannot be directly regarded as effective oxidizer consumption capacity of particles. Figure 11d shows I_{TPCI}, which introduces the oxidizer availability factor F_Y into F_p. This treatment is intended to avoid an overestimated particle combustion potential in regions with very low oxygen content, even when the thermal environment, particle number density, or residence condition is favorable. Therefore, I_{TPCI} emphasizes whether sufficient oxidizer availability is maintained when particles have local oxidizer consumption capability. Compared with the B_2O_2 mass source in Figure 11a, the locations of extreme values and the local intensity distribution of I_{TPCI} are not completely identical, because this index represents particle combustion potential rather than instantaneous reaction source intensity. Nevertheless, from the overall spatial distribution, the high-value regions of I_{TPCI} are generally consistent with the main distribution regions of the actual particle reaction source term. A similar spatial correspondence can be observed in regions influenced by head recirculation, shear interaction, and oxygen replenishment. These results indicate that I_{TPCI} is able to indicate the major potential reaction regions in the baseline afterburner and provide a physically constrained evaluation of particle combustion organization.

Figure 12 further presents the axial evolution of the particle reaction source term, the conventional particle mixing degree, the proposed evaluation indices, and their component factors in the baseline afterburner. Compared with the spatial contours in Figure 11, the axial curves more clearly reveal the streamwise variations in different evaluation quantities and their relationship with the particle reaction region.

As shown in Figure 12a, the B_2O_2 mass source exhibits a pronounced peak near the head region and the air-injection interaction region, followed by an overall decrease in the downstream region, with only a broad secondary response in the middle section. This indicates that particle reaction in the baseline afterburner is mainly concentrated in regions where head recirculation, lateral-injection-induced shear, and oxygen replenishment act together. In contrast, the conventional particle mixing degree continues to increase downstream and gradually approaches a relatively high level in the latter part of the combustor. This trend suggests that, as the particle phase and the oxygen phase further diffuse and are transported downstream, the local two-phase flow-rate ratio may gradually approach the initial mass ratio, which leads to a higher value of β_p. However, the reaction source term does not increase synchronously with β_p. This indicates that ratio matching or transport spreading cannot directly represent the effective particle combustion intensity. The result further suggests that the conventional particle mixing degree is more suitable for identifying local two-phase ratio matching and transport-boundary features, but it is insufficient for independently evaluating particle reaction potential.

Figure 12b compares the axial distributions of the B_2O_2 mass source, F_p, and I_{TPCI}. F_p shows a relatively high response near the head region, indicating that this region has a strong particle-oxidizer consumption capability under the combined effects of gas temperature, particle-number density, residence condition, and particle-thermal reactivity. However, F_p does not directly constrain the local oxidizer availability, and its high value does not necessarily correspond to the peak location of the actual reaction source term. In contrast, I_{TPCI} further introduces F_Y into F_p, thereby reducing the evaluation level in oxygen-deficient regions. It can be observed that the main response region of I_{TPCI} identifies regions that spatially overlap with the main reaction-active regions represented by the

B_2O_2 mass source, particularly in the upstream region dominated by head recirculation and air-injection interaction. In the downstream region, the B_2O_2 mass source still maintains a certain response, whereas I_{TPCI} decreases markedly. This difference reflects the change in the mixing and reaction mode between the upstream and downstream regions. The reaction in the upstream region is mainly controlled by local recirculation, enhanced shear, oxygen replenishment, and particle residence, and therefore exhibits a strongly coupled local feature. In the downstream region, particles and oxygen are transported and diffused over a larger spatial range after the upstream interaction, resulting in a more spatially dispersed reaction contribution. The source-term response in this region therefore mainly reflects the actual consumption process between the post-mixing residual particles and oxidizer. By contrast, I_{TPCI} tends to identify favorable potential regions where particle oxidizer consumption capability and oxidizer availability coexist. It therefore gives a lower evaluation in the downstream region. This result indicates that I_{TPCI} is not a direct substitute for the instantaneous reaction source intensity, but is instead intended to identify regions that are more favorable for sustained particle combustion under the current flow organization.



(**a**) Mass source vs. β_p

(**b**) Mass source vs. F_p vs. I_{TPCI}

(**c**) Factors (Particles)

(**d**) Factors (Gas)

Figure 12. Axial evolution of combustion source and evaluation quantities.

Figure 12c,d further present the axial evolution of the component factors in F_p and I_{TPCI}, which helps explain the difference between the evaluation indices and the reaction source term in Figure 12b. Overall, the head region has relatively high particle thermal

reactivity, a strong local residence advantage, and a more mature thermal environment. Therefore, F_{T_p}, F_v, and F_T jointly support a high particle-oxidizer consumption capability in this region. This is consistent with the spatial distribution in Figure 11, where the high value region of F_p is mainly concentrated in the head recirculation region. This result indicates that head recirculation not only extends the particle residence time but also provides favorable conditions for particle heating and local reaction. In the lateral jet interaction region, the factor variations reflect the competition between oxygen replenishment and thermal-environment deterioration. F_Y increases significantly after air injection, indicating that the air inlets effectively enhance the local oxidizer availability. At the same time, the introduction of relatively cold lateral air reduces the local gas temperature and causes a decrease in F_T. The particle-related factors are also affected by jet interaction and main-flow shear, and the particle thermal state and local particle distribution no longer remain at the favorable level observed in the head region. Therefore, although the jet interaction region improves oxygen supply and two-phase transport conditions, it does not necessarily produce the highest particle combustion potential. This phenomenon indicates that increasing oxidizer availability alone is insufficient to enhance I_{TPCI}. The thermal environment and particle state remain important constraints on the effective reaction potential in this region. In the downstream main-flow development region, the factor variations further reveal the attenuation mechanism of reaction potential after distributed transport. The gradual increase in F_n mainly indicates that the particle cloud expands its spatial coverage after the upstream recirculation and jet interaction, so that more cells within each section contain appreciable particle number density. It should not be interpreted as an increase in the total particle amount along the streamwise direction. Meanwhile, F_{T_p}, F_T, and F_v remain relatively constrained downstream, indicating that the particle thermal state, gas-phase thermal environment, and local residence advantage are not maintained in parallel with oxygen replenishment. Consequently, although particle transport and oxidizer availability still exist downstream, F_p and I_{TPCI} do not show the continuously increasing trend observed for β_p. This result indicates that the downstream combustion potential is limited by the incomplete conversion of transport and oxidizer availability into effective particle reaction conditions.

Figure 13 further analyzes the role of different physical factor groups in I_{TPCI} from the perspective of regional contribution. To distinguish the effects of oxygen particle-transport conditions and thermal-environment conditions on particle combustion potential, I_{TPCI} is decomposed into two factor groups. The first group is the oxygen particle transport factor group.

$$F_{\mathrm{OP}} = F_Y F_v F_n \tag{41}$$

which combines oxidizer availability, local residence condition, and particle number density availability. It is therefore used to describe the encounter, transport, and supply potential of oxygen and particles in the flow organization. The second group is the thermal-environment factor group.

$$F_{\mathrm{TE}} = F_T F_{T_p} \tag{42}$$

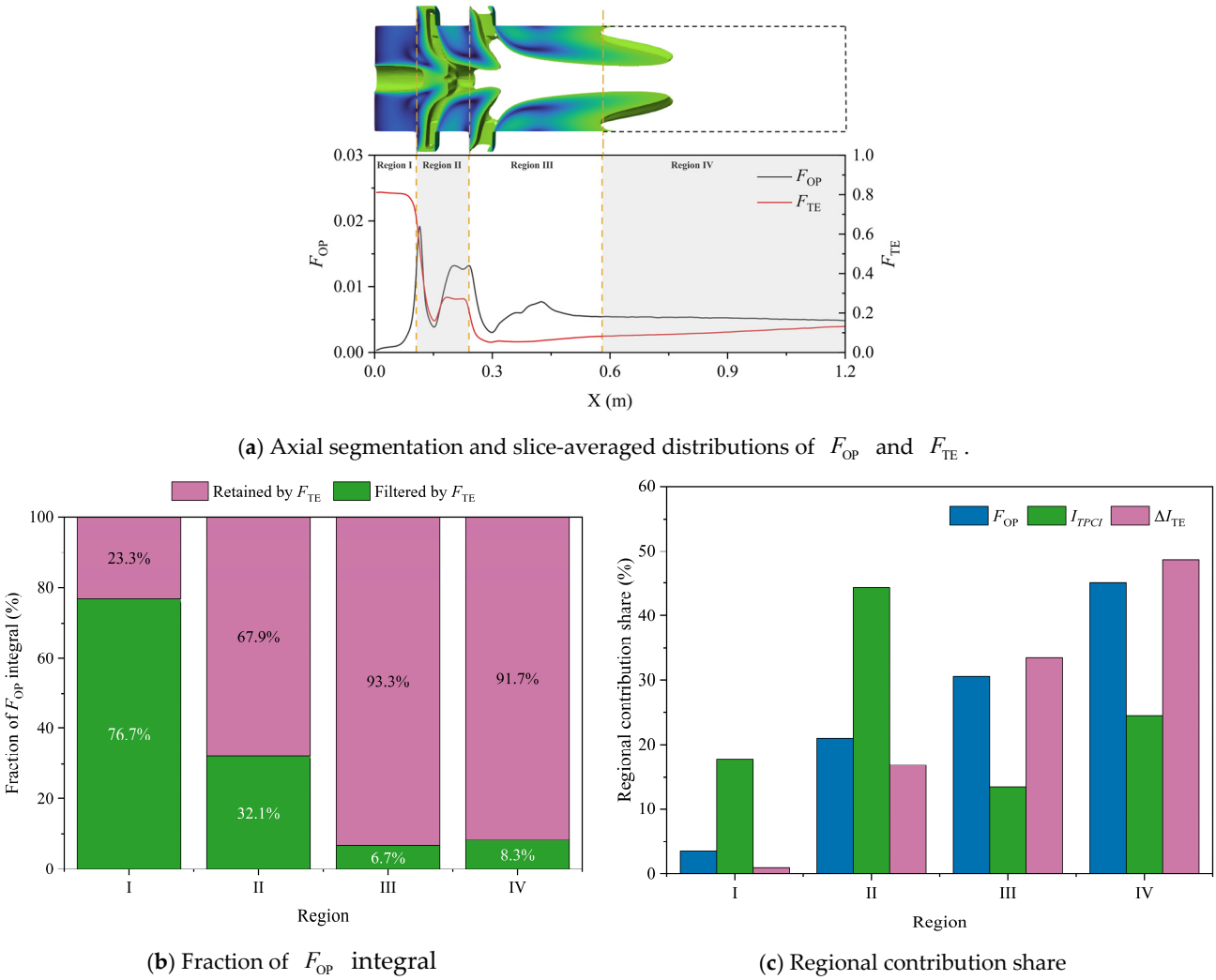
which consists of the gas temperature factor and the particle thermal reactivity factor. It is used to describe whether the local gas thermal environment and particle thermal state are favorable for particle reaction.

This grouping does not redefine a new evaluation index. Instead, it is introduced to explain the regional differences in I_{TPCI} from the perspective of physical mechanisms. Specifically, F_{OP} represents the potential reaction basis provided by oxygen particle transport and supply conditions, whereas F_{TE} represents the retention or suppression effect of the thermal

environment on this potential. To quantify the filtering effect of the thermal environment on the oxygen particle transport potential, the following quantity is further defined.

$$\Delta I_{\mathrm{TE}} = F_{\mathrm{OP}} - I_{TPCI} = F_{\mathrm{OP}}(1 - F_{\mathrm{TE}}) \tag{43}$$

where ΔI_{TE} represents the portion of the potential that is formed by oxygen particle transport conditions but is not retained as I_{TPCI} because of insufficient thermal environment. It should be emphasized that ΔI_{TE} does not represent the loss of the reaction source term. Rather, it describes the filtering intensity of the thermal-environment factor on the potential particle combustion region.



(**a**) Axial segmentation and slice-averaged distributions of F_{OP} and F_{TE}.

(**b**) Fraction of F_{OP} integral

(**c**) Regional contribution share

Figure 13. Regional contribution analysis of the grouped factors in the baseline afterburner.

Figure 13a shows the axial segmentation used for the regional statistics, together with the section-averaged distributions of F_{OP} and F_{TE}. Based on the flow structure characteristics, the baseline afterburner is divided into four axial regions. These regions correspond to the head region, the primary air injection region, the secondary air injection region and its downstream low-speed wake-influence region, and the downstream main-flow development region. The boundary between Regions III and IV is placed at the downstream closure of the secondary jet-induced low-speed wake, which is represented by the median velocity envelope of the effective afterburner flow region. For the present baseline case, the corresponding velocity is approximately (135 m/s). It can be seen that F_{TE} remains at a

high level in the head region, indicating that this region has a relatively mature thermal environment and a favorable particle thermal state. In contrast, F_{OP} is relatively low in the head region, indicating that the oxygen particle transport and supply potential has not been fully established, although the thermal environment is favorable. After entering the primary and secondary air injection regions, F_{OP} increases significantly, suggesting that lateral air injection promotes oxidizer replenishment and two-phase transport organization. However, F_{TE} decreases after air injection, reflecting the weakening of the local thermal environment caused by the introduction of cold air. Therefore, Figure 13a shows that the oxygen particle transport condition and the thermal-environment condition do not evolve synchronously in different axial regions. This is the reason why I_{TPCI} needs to include both F_{OP} and F_{TE}.

Figure 13b further shows the retained and filtered fractions of F_{OP} by the thermal environment in each region. For the r-th region, the retained fraction is defined as

$$\phi_{\mathrm{ret}}^{(r)} = \frac{\int_{\Omega_r} I_{TPCI} dV}{\int_{\Omega_r} F_{\mathrm{OP}} dV} \tag{44}$$

and the filtered fraction is defined as

$$\phi_{\mathrm{fil}}^{(r)} = \frac{\int_{\Omega_r} \Delta I_{\mathrm{TE}}, dV}{\int_{\Omega_r} F_{\mathrm{OP}}, dV} \tag{45}$$

The sum of these two fractions is equal to unity. This figure indicates, within each region, how much of the potential reaction basis formed by oxygen particle transport is retained as the complete I_{TPCI}, and how much is weakened by thermal-environment limitations. The results show that Region I has the highest retained fraction, approximately 76.7%. This indicates that although the total amount of F_{OP} is not high in the head region, most of the oxygen particle transport potential can be retained by the relatively mature thermal environment once it is formed. The retained fraction in Region II decreases to approximately 32.1%, indicating that the primary air injection region significantly enhances the transport potential, while part of this potential is limited by cold air introduction and thermal-environment deterioration. The retained fractions in Regions III and IV are approximately 6.7% and 8.3%, respectively. This indicates that, in the secondary air injection wake region and the downstream main-flow region, a considerable oxygen particle transport potential still exists, but most of it is not converted into thermal-environment-constrained particle combustion potential.

Figure 13c compares the contribution of different regions to the total integrated values of F_{OP}, I_{TPCI}, and ΔI_{TE}. For an arbitrary quantity Q, the regional contribution share is defined as

$$C_Q^{(r)} = \frac{\int_{\Omega_r} Q, dV}{\sum_r \int_{\Omega_r} Q, dV} \tag{46}$$

where Q can be F_{OP}, I_{TPCI}, or ΔI_{TE}. The results show that the contribution of F_{OP} mainly comes from Regions III and IV, whose combined share exceeds 75%. This indicates that the downstream regions provide a larger oxygen particle transport potential in terms of spatial extent. However, the largest contribution to I_{TPCI} comes from Region II, accounting for approximately 44.3%, followed by Regions IV and I. This suggests that the transport potential in the primary air injection region is more readily retained by the thermal environment and converted into a higher comprehensive particle combustion potential. At the same time, the contribution of ΔI_{TE} mainly comes from Regions III and IV, with shares of approximately 33.5% and 48.7%, respectively. This indicates that the secondary air injection wake region

and the downstream main-flow region are the regions where the thermal-environment filtering effect is strongest.

Overall, Figure 13 shows that the particle combustion potential in the baseline afterburner is not simply determined by oxygen replenishment or enhanced particle transport. The head region has a relatively mature thermal environment, but the oxygen particle transport potential is limited. The primary air injection region enhances oxidizer supply while maintaining a certain level of thermal-environment support, and therefore makes the most prominent contribution to I_{TPCI}. Although the secondary air injection region and the downstream main-flow region provide a wider distribution of F_{OP}, a considerable portion of this potential is identified by ΔI_{TE} as transport potential that is not retained because of the thermal-environment limitation. This regional analysis further demonstrates that I_{TPCI} can identify not only the encounter and transport conditions between particles and oxidizer, but also the regions where transport advantages can be converted into effective particle-combustion potential under thermal-environment constraints.

4. Application to Pulsed-Jet Flow-Control Evaluation

To evaluate the applicability of the proposed framework in flow-control design, pulsed air jets were introduced into the baseline afterburner. As shown in Figure 14, five candidate actuation locations, denoted as Point 1 to Point 5, were selected according to the main-flow structures and the available installation space. For each controlled case, a pair of symmetrically arranged pulsed-jet inlets was placed at one selected location, while the other geometric and operating conditions were kept identical to those of the baseline case. The pulsed jet was specified as a non-suction sinusoidal air injection, expressed as

$$\dot{m}_j(t) = \frac{A}{2}[1 + \sin(2\pi f t)] \tag{47}$$

where A = 0.008 kg/s is the mass-flow-rate amplitude of each jet orifice and f = 200 Hz is the actuation frequency. Since the actuation flow rate is much lower than the original air-inlet flow rate, the pulsed jets are intended to modify the local flow organization rather than change the global oxidizer supply level.

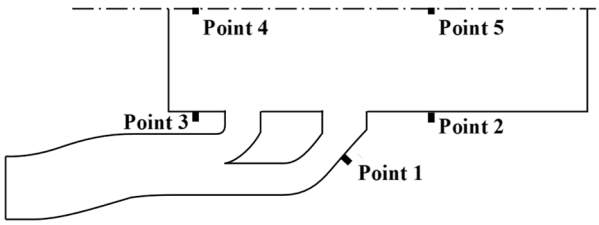


Figure 14. The position of the pulsed jet injector.

Accordingly, five controlled cases were defined as Case P1 to Case P5, corresponding to pulsed-jet actuation at Points 1 to 5, respectively. In all cases, the actuation frequency and mass-flow-rate amplitude were kept unchanged, so that the differences among the controlled cases only reflect the effect of actuation location.

Since all pulsed-jet cases introduce the same additional air supply and use the same waveform, frequency, and maximum jet mass flow rate, Cases P1–P5 can be compared with each other to examine the influence of actuation location. Among them, P1 is located at the inlet side and is therefore used as a pulsed-inlet reference case. Cases P2–P5 are mounted on the afterburner wall and are compared with P1 to identify whether local wall actuation provides additional benefits beyond inlet-side pulsed air addition. After the wall-actuation location exhibiting the most favorable response is identified, its response

is further compared with the uncontrolled baseline case to evaluate the influence of local flow control.

Figure 15 presents the phase-resolved local I_{TPCI} contours near the pulsed-jet actuation locations for Cases P1–P5. The local slice plane is selected according to the orientation of the corresponding pulsed-jet inlet, and all panels use the same color scale as that in Figure 11d. Compared with the baseline distribution, the responses of Cases P1 and P2 are relatively limited, and no evident expansion of the high-I_{TPCI} region can be observed near the head region. In contrast, Cases P3 and P4 produce a much stronger enhancement of I_{TPCI} in the head region, indicating that the pulsed jets at these two locations can more effectively interact with the local recirculation and oxygen replenishment structures. Case P5 mainly induces a weak downstream response, while its influence on the high-potential head region remains limited. These phase-resolved contours indicate that P3 and P4 have a stronger potential to enhance the head-region I_{TPCI}, whereas P5 only produces a weak downstream response. A cycle-averaged regional comparison is therefore required to further evaluate the relative effectiveness of different actuation locations.

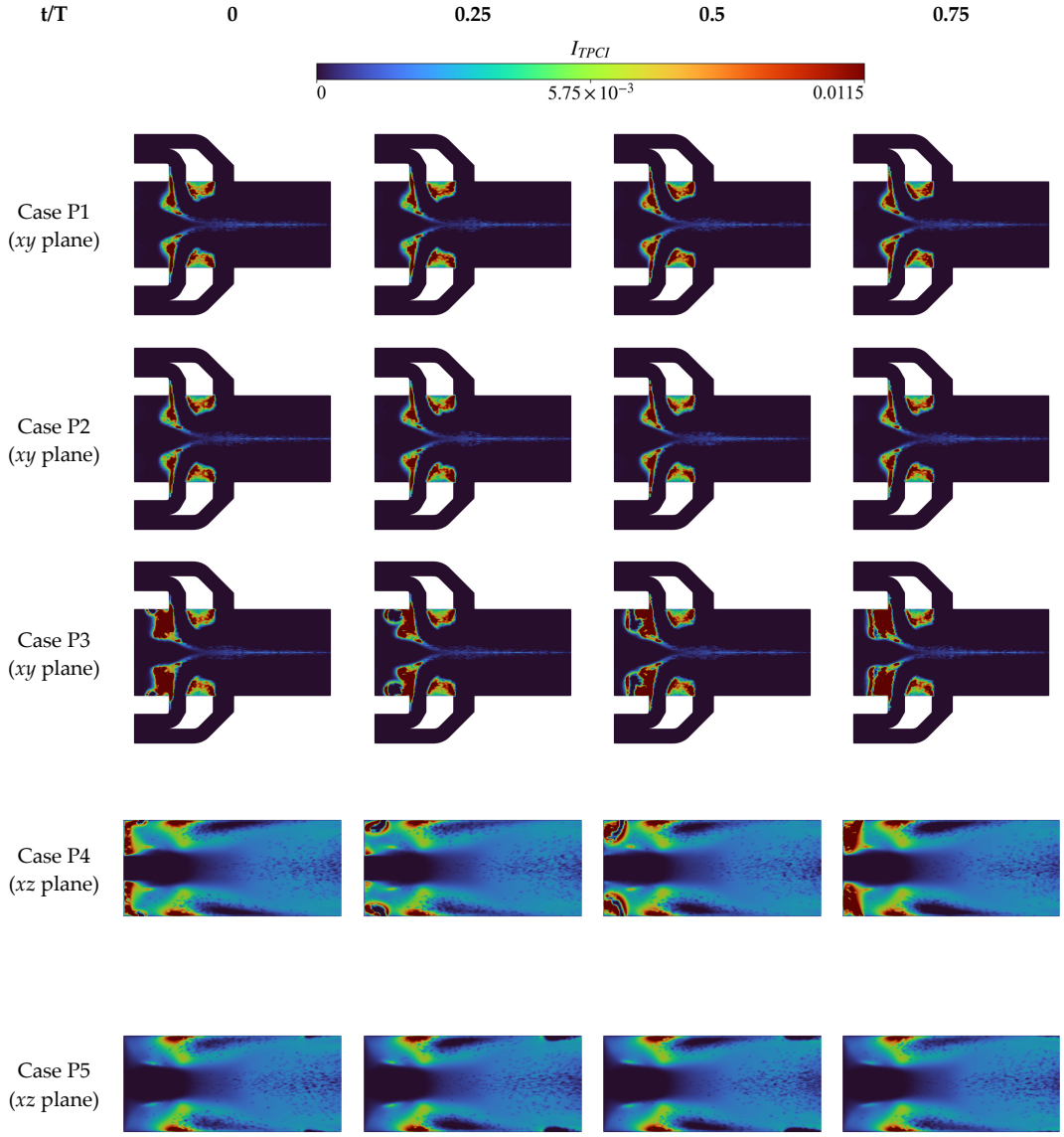


Figure 15. Local I_{TPCI} contours for Cases P1–P5. (The local slice plane may be *xy* or *xz*, depending on the orientation of the corresponding pulsed-jet inlet. The value range of I_{TPCI} is [0, 0.0115], which is consistent with Figure 11d).

Since the pulsed-jet actuation introduces periodic unsteadiness, the regional I_{TPCI} response is evaluated using time-averaged values rather than instantaneous values. After the flow reaches a statistically periodic state, the sampled data over three complete actuation periods are averaged to reduce the influence of cycle-to-cycle fluctuations while retaining the mean effect of the pulsed actuation. The resulting cycle-averaged regional values are used for the comparison in Figure 16. In Region I, Cases P3 and P4 exhibit much higher I_{TPCI} than P1, P2, and P5, indicating that these two wall-mounted actuation locations exhibit a more favorable response in enhancing the head-region particle combustion potential. In Region II, all cases show relatively high values, and P3 gives the highest response, although the difference among the cases is less pronounced than that in Region I. In Regions III and IV, the absolute I_{TPCI} levels are much lower, as shown more clearly in the inset. Although P5 shows a slight advantage in Region IV, its enhancement is limited to the downstream low-potential region. Considering that P3 provides a strong enhancement in the head region and maintains a relatively balanced response in the other regions, it is selected for the subsequent comparison with the uncontrolled baseline case.

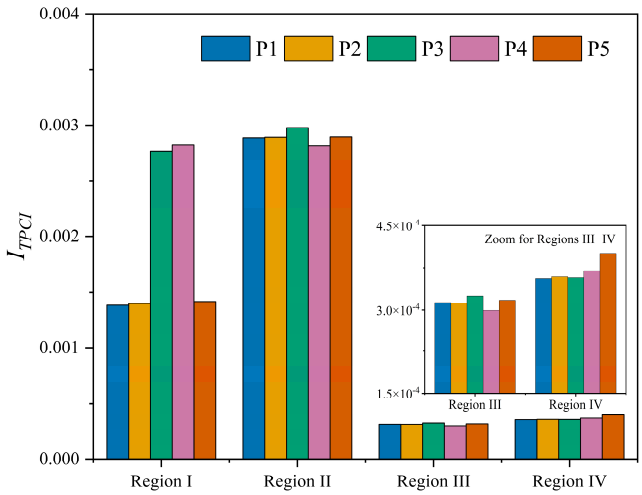


Figure 16. Cycle-averaged regional I_{TPCI} responses of the pulsed-jet cases P1–P5.

Figure 17 further compares the axial distributions of the cycle-averaged I_{TPCI} and B_2O_2 mass source between the baseline case and case P3. Compared with the baseline case, P3 produces a pronounced increase in I_{TPCI} in the head region, whereas the enhancement becomes much weaker in the downstream jet-interaction and main-flow regions. A similar trend can also be observed in the B_2O_2 mass source distribution, although its response is more moderate than that of I_{TPCI}. This indicates that the main effect of P3 is not to uniformly strengthen particle combustion over the entire afterburner, but to significantly improve the upstream high-potential combustion region and moderately enhance the downstream reaction-source level.

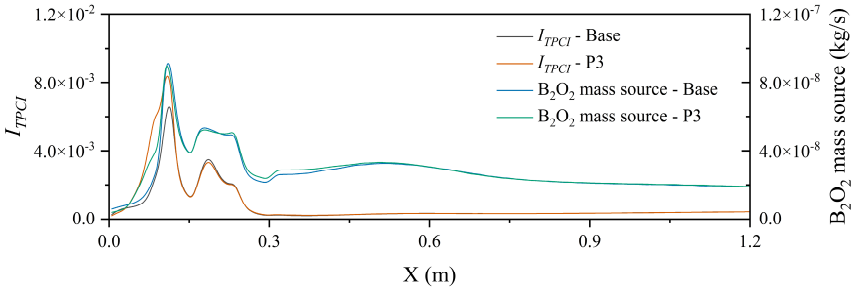


Figure 17. Comparison of axial I_{TPCI} and B_2O_2 mass source between the baseline and case P3.

The regional integral results further compare the relative improvements of P3, P4, and P5 over the baseline case in the head region (Region I), jet-interaction region (Region II + III), and downstream main-flow region (Region IV), as summarized in Table 7. For the upstream-actuated cases P3 and P4, the enhancement is mainly concentrated in the head region, indicating that pulsed jets placed near the upstream high-potential zone can effectively strengthen the local particle-combustion response. However, P4 also weakens the jet-interaction region, so that its full-domain source-term enhancement is only 0.97%, much lower than the 2.96% obtained by P3, despite its stronger head-region response and slight improvement in the downstream main-flow region. In contrast, the improvement produced by P5 is mainly confined to the downstream main-flow region. Its enhancement of I_{TPCI} is more evident downstream, while the corresponding source-term response remains moderate, giving a full-domain source-term enhancement of 2.11%.

Table 7. Relative changes in regional-mean values for P3, P4, and P5 with respect to the baseline.

Quantity	Region	P3	P4	P5
I_{TPCI}	Head region	+97.07%	+100.83%	+1.18%
I_{TPCI}	Jet-interaction region	+3.47%	−2.78%	+0.71%
I_{TPCI}	Downstream main-flow region	−0.50%	+2.98%	+11.52%
I_{TPCI}	Full domain	+18.55%	+16.52%	+3.57%
B_2O_2 mass source	Head region	+29.20%	+42.64%	+0.64%
B_2O_2 mass source	Jet-interaction region	+2.16%	−4.94%	+0.80%
B_2O_2 mass source	Downstream main-flow region	+0.28%	+2.39%	+3.93%
B_2O_2 mass source	Full domain	+2.96%	+0.97%	+2.11%

Overall, the comparison indicates that the variation of I_{TPCI} can provide a useful indication of the change in particle source-term intensity under pulsed-jet actuation. Oxygen-supplementing enhancement of combustion potential in both the head recirculation region and the downstream region (high-temperature oxygen-lean) can modify the B_2O_2 mass source distribution, while the response in the head region is much stronger than that in the downstream region. For the present configuration, placing the head-region pulsed jet on the side opposite to the original inlet weakens the particle combustion response in the jet-interaction region, whereas placing the downstream pulsed jet on the opposite side of the original inlet can improve the subsequent downstream combustion response.

5. Conclusions

In this study, a thermal-environment-informed particle combustion index I_{TPCI} was proposed to diagnose particle combustion organization in solid rocket ramjet afterburners. The proposed index is constructed as a flow-field-based diagnostic quantity to identify how local flow organization and thermochemical conditions contribute to variations in particle combustion behavior. By incorporating oxidizer availability, particle–oxidizer transport, residence-related effects, gas thermal environment, and particle thermal reactivity, I_{TPCI} provides a combustion-potential-oriented description of reacting particle-laden flows.

The comparison between the conventional particle mixing degree and I_{TPCI} reveals that these two quantities characterize different physical aspects of reacting particle flows. The conventional particle mixing degree mainly identifies regions where the local particle-to-oxidizer ratio approaches the initial feeding condition, corresponding to particle–oxidizer transport interfaces or shear-layer-dominated mixing boundaries. However, these regions do not necessarily correspond to regions with high particle combustion potential because heterogeneous particle reactions are constrained by reaction kinetics, particle thermal state, residence condition, and local thermal environment. In contrast, I_{TPCI} identifies regions where particle oxidizer-consumption capability can be retained under favorable flow and thermochemical conditions. The baseline afterburner analysis further shows that particle

combustion organization is determined by the coupled interaction among oxidizer supply, gas–solid transport, residence characteristics, and thermal environment, rather than by oxidizer replenishment or particle dispersion alone.

The application of I_{TPCI} to pulsed-jet flow control demonstrates its capability for interpreting combustion-performance variations from the perspective of regional contribution. For the present configuration and operating condition, the enhancement induced by pulsed actuation is mainly associated with the modification of local flow organization and oxidizer supply in specific regions rather than a uniform improvement throughout the afterburner. The results further indicate that the relative arrangement between the pulsed actuator and the original flow structures plays an important role in determining the combustion response. Specifically, under the investigated conditions, upstream pulsed jets tend to produce a more favorable response when arranged on the same side as the original inlet, whereas downstream pulsed jets show a more favorable response when arranged on the opposite side of the original inlet. These observations provide a diagnostic basis for actuator-location optimization under the investigated conditions. The present index is established within the adopted gas–solid reaction model and the investigated afterburner configuration. Further validation under different operating conditions and configurations is required to assess its broader applicability.

Author Contributions: Conceptualization, D.S. and L.S.; methodology, D.S.; software, D.S.; validation, X.L. and C.G.; formal analysis, D.S. and X.L.; investigation, L.S. and X.L.; resources, F.B. and L.S.; data curation, C.G.; writing—original draft preparation, D.S.; writing—review and editing, L.S. and F.B.; visualization, D.S.; supervision, F.B.; project administration, F.B.; funding acquisition, L.S. All authors have read and agreed to the published version of the manuscript.

Funding: This research was funded by the National Natural Science Foundation of China, grant number 52302479.

Data Availability Statement: The data that support the findings of this study are available from the corresponding author upon reasonable request.

Conflicts of Interest: The authors declare no conflicts of interest. The funders had no role in the design of the study; in the collection, analyses, or interpretation of data; in the writing of the manuscript; or in the decision to publish the results.

References

1. Fry, R.S. A Century of Ramjet Propulsion Technology Evolution. *J. Propuls. Power* **2004**, *20*, 27–58. [CrossRef]
2. Besser, H. History of Ducted Rocket Development at Bayern-Chemie. In *44th AIAA/ASME/SAE/ASEE Joint Propulsion Conference & Exhibit*; American Institute of Aeronautics and Astronautics: Reston, VA, USA, 2008; p. 5261. [CrossRef]
3. Stowe, R.A.; Dubois, C.; Harris, P.G.; Mayer, A.E.H.J.; de Champlain, A.; Ringuette, S. Performance Prediction of a Ducted Rocket Combustor Using a Simulated Solid Fuel. *J. Propuls. Power* **2004**, *20*, 936–944. [CrossRef]
4. Huang, W.; Li, M.; Yan, L. Mixing Augmentation Mechanism Induced by the Pseudo Shock Wave in Transverse Gaseous Injection Flow Fields. *Int. J. Hydrogen Energy* **2016**, *41*, 10961–10968. [CrossRef]
5. Liu, J.; Wang, N.; Wang, J.; Li, Z. Optimizing Combustion Performance in a Solid Rocket Scramjet Engine. *Aerosp. Sci. Technol.* **2020**, *99*, 105560. [CrossRef]
6. Yang, P.; Xia, Z.; Ma, L.; Chen, B.; Feng, Y.; Li, C.; Zhao, L. Influence of the Multicavity Shape on the Solid Scramjet. *Int. J. Aerosp. Eng.* **2021**, *2021*, 9718537. [CrossRef]
7. Zhang, J.; Lin, L.; Yong, K.; Bao, W. Influence of Incident Shocks on Flame Characteristics in the Strut-Equipped Supersonic Combustor. *AIAA J.* **2023**, *61*, 76–85. [CrossRef]
8. Zhang, D.; Cui, P.; Tan, J.; Yao, X. Mixing Enhancement of Supersonic Flow Induced by Splitter Plate Cavity. *Aerosp. Sci. Technol.* **2022**, *128*, 107742. [CrossRef]
9. Ogawa, H. Mixing Characteristics of Inclined Fuel Injection via Various Geometries for Upstream-Fuel-Injected Scramjets. *J. Propuls. Power* **2015**, *31*, 1551–1566. [CrossRef]

10. Sheng, Z.; Zhang, L.; Dan, Y.; Wang, Y. Configuration of the Lobed Nozzle in an Ejector Mixer for Extreme Mixing Efficiency. *Int. J. Heat Mass Transf.* **2022**, *183*, 122102. [CrossRef]
11. Rao, A.N.; Kushari, A.; Jaiswal, G.K. Effect of Nozzle Geometry on Flowfield for High Subsonic Jets. *J. Propuls. Power* **2018**, *34*, 1596–1608. [CrossRef]
12. Ko, T.H. Three-Dimensional Fuel–Air Mixing Phenomena in a Side-Dump Combustor: A Numerical Study. *Int. Commun. Heat Mass Transf.* **2005**, *32*, 1360–1374. [CrossRef]
13. Zhang, Y.; Wu, Z.; Zhang, Z.; Chen, P.; Niu, Y.; Chen, X.; He, Y.; Fang, G. Effect of Gas Injection Holes on Mixing and Combustion in Solid Propellant Ducted Rockets. *Appl. Therm. Eng.* **2023**, *226*, 120212. [CrossRef]
14. Zhang, Y.; Wu, Z.; Zhang, Z.; Chen, P.; Chang, Y.; Zhang, X.; Chen, X. Effect of Synergistic Impact Gas Injection Device on Secondary Combustion in Boron-Based Ducted Rockets. *Appl. Therm. Eng.* **2024**, *242*, 122558. [CrossRef]
15. Shin, J. Characteristics of High Speed Electro-Thermal Jet Activated by Pulsed DC Discharge. *Chin. J. Aeronaut.* **2010**, *23*, 518–522. [CrossRef]
16. Ali, M.; Ahmed, K.; Kumar, R.; Alvi, F. Flow Field Characteristics of Oblique Shocks Generated Using Microjet Arrays. *Int. J. Flow Control* **2014**, *6*, 93–109. [CrossRef]
17. Ahmed, K.A.; Ali, M.Y.; Alvi, F.S. Mixing Characteristics of Active Microjet-Based Actuators in a Supersonic Backward-Facing-Step Flow. *AIAA J.* **2014**, *52*, 2855–2866. [CrossRef]
18. Hiejima, T.; Oda, T. Shockwave Effects on Supersonic Combustion Using Hypermixer Struts. *Phys. Fluids* **2020**, *32*, 016104. [CrossRef]
19. Eri, Q.; Hong, L.; Li, T.; Wang, Q.; Wang, M. Numerical Simulations of Mixing Enhancement in Subsonic Jet Using High-Momentum Synthetic Jets. *J. Propuls. Power* **2016**, *32*, 1095–1103. [CrossRef]
20. Papamoschou, D.; Roshko, A. The Compressible Turbulent Shear Layer: An Experimental Study. *J. Fluid Mech.* **1988**, *197*, 453–477. [CrossRef]
21. Ding, H.; Zhuo, C.; Chen, X.; Deng, H.; Li, M.; Sun, B.; Li, C. Numerical Study on the Transverse Jet Flow and Mixing Characteristics of Hydrogen/Metal Powder Fuel in Powder Fuel Scramjet. *Fuel* **2022**, *326*, 125088. [CrossRef]
22. Yamashita, H.; Shimada, M.; Takeno, T. A Numerical Study on Flame Stability at the Transition Point of Jet Diffusion Flames. *Symp. (Int.) Combust.* **1996**, *26*, 27–34. [CrossRef]
23. Mao, M.; Riggins, D.; McClinton, C. Numerical Simulation of Transverse Fuel Injection. In *Proceedings of the NASA, Lewis Research Center, Computational Fluid Dynamics Symposium on Aeropropulsion*; NASA: Washington, DC, USA, 1990; Volume 1, pp. 635–667.
24. Sislian, J.; Schumacher, J. Fuel/Air Mixing Enhancement by Cantilevered Ramp Injectors in Hypersonic Flows. In *Proceedings of the International Society for Air Breathing Engines-ISOABE, ISABE-International Symposium on Air Breathing Engines, 14th*; International Society for Air Breathing Engines (ISABE): Indianapolis, IN, USA, 1999.
25. Chen, B.; Xia, Z.; Wang, D.; Hu, J.; Ma, L.; Zhao, X. Study on Mixing Process Assessment Method in Solid Ramjet. *J. Solid Rocket Technol.* **2013**, *36*, 731–735. [CrossRef]
26. Bian, F.; Sun, L.; Shi, D.; Bao, F. An Efficient Approach for Computing the Finite Time Lyapunov Exponent in Complex Three-Dimensional Flow Based on the Discrete Phase Model. *Aerosp. Sci. Technol.* **2023**, *133*, 108110. [CrossRef]
27. Sun, L.; Bian, F.; Lei, X.; Shi, D.; Bao, F. Quantitative Analysis of Enhanced Mixing and Combustion by Lobed Mixer in a Ramjet Engine: Study Using Hyperbolic Lagrangian Coherent Structures. *Aerosp. Sci. Technol.* **2023**, *140*, 108471. [CrossRef]
28. Xu, Y.; Jia, R.; Medina, H.; Sun, H. Effect of Tangential Swirl Air Inlet Angle on the Combustion Efficiency of a Hybrid Powder-Solid Ramjet. *Acta Astronaut.* **2019**, *159*, 87–95. [CrossRef]
29. Cao, D.; He, G.; Qin, F.; Michaels, D. Local Supersonic and Subsonic Combustion Mode Transition in a Supersonic Jet Flame. *Proc. Combust. Inst.* **2019**, *37*, 3723–3731. [CrossRef]
30. Li, W.; Zhao, D.; Chen, X.; Zhu, L.; Ni, S. Numerical Investigation of Inlet Thermodynamic Conditions on Solid Fuel Ramjet Performances. *Int. J. Aerosp. Eng.* **2021**, *2021*, 8868288. [CrossRef]
31. Wu, X.; Wei, Z.; Wang, Y.; Zhou, L.; Wang, Y.; Wang, N. Performance Comparison of Full-Scale Ramjet and Scramjet Using Boron-Based Propellant. *Def. Technol.* **2026**, *56*, 206–217. [CrossRef]
32. Ulas, A.; Kuo, K.K.; Gotzmer, C. Ignition and Combustion of Boron Particles in Fluorine-Containing Environments. *Combust. Flame* **2001**, *127*, 1935–1957. [CrossRef]
33. Kuo, K.; Acharya, R. *Applications of Turbulent and Multiphase Combustion*; John Wiley & Sons: Hoboken, NJ, USA, 2012.
34. Park, J.S.; Park, S.S.; Han, D.-H.; Sung, H.-G.; Kwak, J.S.; Choi, H.-J. Flow Characteristics in a Rectangular Mixing Chamber with Two Jets. *J. Propuls. Power* **2016**, *32*, 456–462. [CrossRef]

Disclaimer/Publisher's Note: The statements, opinions and data contained in all publications are solely those of the individual author(s) and contributor(s) and not of MDPI and/or the editor(s). MDPI and/or the editor(s) disclaim responsibility for any injury to people or property resulting from any ideas, methods, instructions or products referred to in the content.